UNIVERSITY OF OKLAHOMA
GRADUATE COLLEGE

AN IMAGING SYSTEM TO STUDY SPIN DYNAMICS IN ULTRACOLD SODIUM GASES

A THESIS

SUBMITTED TO THE GRADUATE FACULTY
in partial fulfillment of the requirements for the
Degree of
MASTER OF SCIENCE

By

NANDITA TALUKDER MUNNA

Norman, Oklahoma

2026

Downloaded from SHAREOK. Persistent Handle URL: https://hdl.handle.net/11244/342812

AN IMAGING SYSTEM TO STUDY SPIN DYNAMICS IN ULTRACOLD SODIUM GASES

A THESIS APPROVED FOR THE

DEPARTMENT OF ENGINEERING PHYSICS

By The Committee Consisting of

Dr. Arne Schwettmann, Chair

Dr. Eric Abraham

Dr. Mike Santos

© Copyright by NANDITA TALUKDER MUNNA 2026
All Rights Reserved.

Acknowledgements

I would like to express my deepest gratitude to my advisor, **Dr. Arne Schwettmann**, for his invaluable guidance, patience, and unwavering support throughout my master's research. His enthusiasm for experimental atomic physics, thoughtful mentorship, and encouragement to approach scientific problems with curiosity and rigor have profoundly shaped my development as a researcher. I am sincerely grateful for the opportunity to work in his laboratory and learn from his expertise.

I am also deeply thankful to my committee members, **Dr. Eric Abraham** and **Dr. Mike Santos**, for generously sharing their time, valuable suggestions, and insightful feedback throughout this work. Their perspectives have helped strengthen both this thesis and my understanding of experimental physics. I would also like to thank Dr. **John Moore-Furneaux** for his continuous support thorughout this journey. I would like to sincerely thank my labmates, **Sankalp**, **Hio**, **Cordellia**, and **Sam**, for creating a collaborative and enjoyable research environment. Their willingness to help, share ideas, and engage in countless scientific discussions made my time in the laboratory both productive and memorable.

I am forever grateful to my parents for their unconditional love, sacrifices, and unwavering faith in my dreams. Their encouragement and support have been the foundation upon which every achievement in my life has been built. I would also like to thank my sisters for their constant love, encouragement, and for always reminding me that home is never far away.

Finally, and most importantly, I wish to express my heartfelt gratitude to my beloved husband, **Himel Talukder**. His unwavering love, patience, encouragement, and constant belief in me have been my greatest source of strength throughout this journey.

This material is based upon work supported by the National Science Foundation under Grant Number PHY-2513399. Any opinions, findings, and conclusions or recommendations expressed in this material are those of the author(s) and do not necessarily reflect the views of the National Science Foundation.

Contents

Acknowledgements iv

List of Figures vii

List of Tables xii

Abstract xiii

1 Introduction 1

2 Background and Theoretical Framework 4

2.1 Laser Cooling, Trapping, and Sodium MOT 4

2.2 Optical System Design for High Precision Imaging 5

2.3 Absorption Imaging Theory and Measurement Accuracy 6

2.4 Resolution, Optical Performance Metrics 6

2.5 Spinor Quantum Gas Theory 8

3 Experimental Set Up for Cooling and Trapping 12

3.1 Introduction 12

3.2 Overview of the Experimental Apparatus 13

3.2.1 Ultra-High Vacuum Assembly 14

3.2.2 Thermal Sodium Source 16

3.2.3 Zeeman Slower 17

3.2.4 Main Experimental Chamber 19

3.2.5 Magnetic Field Control System 20

3.3 Laser System Setup 23

3.3.1 Laser Beam Distribution 24

3.3.2 AOMs and Mechanical Shutters 28

4 Imaging System Design **30**

4.1 Introduction . . . 30

4.2 Theoretical Background . . . 31

4.2.1 Optical Resolution . . . 31

4.2.2 Absorption Imaging . . . 32

4.3 Optical Design of the Imaging System . . . 34

4.4 Implementation of the Imaging System . . . 37

5 Imaging System Characterization **39**

5.1 Introduction . . . 39

5.2 Experimental Image Acquisition . . . 39

5.3 Analysis of the Obtained Images . . . 41

5.3.1 Magnification Measurement . . . 41

5.3.2 Intensity Profile Analysis . . . 43

5.3.3 Resolution Assessment with Rayleigh Criterion . . . 46

6 Discussion and Conclusions **50**

6.1 Discussion . . . 50

6.2 Performance of the Imaging System . . . 51

6.3 Limitations of the Current Imaging System . . . 54

6.4 Outlook and Future Work . . . 54

6.5 Conclusions . . . 55

List of Figures

2.1 (a) Schematic representation of spatially varying Zeeman energy shifts, illustrating position-dependent resonance conditions and the preferential absorption of oppositely circularly polarized light across the trapping region. (b) Schematic illustration of a magneto-optical trap (MOT) consisting of six counter-propagating laser beams and a pair of coils in an anti-Helmholtz configuration, generating a quadrupole magnetic field with a zero-field point at the trap center. 5

2.2 Energy level structure of the sodium D_2 transition. 7

2.3 Schematic illustration of the criterion for Bose–Einstein condensation. 8

2.4 Schematic illustration of spin-changing collisions in an $F = 1$ sodium spinor Bose–Einstein condensate. Two atoms initially occupying the $m_F = 0$ state collide through spin-exchange interactions and are converted into correlated atoms in the $m_F = +1$ and $m_F = -1$ states while conserving total magnetization. The process is analogous to optical four-wave mixing and generates quantum correlations between the two output states. 9

2.5 (a) Spin-changing collisions in an $F = 1$ sodium spinor condensate driven by spin-exchange interactions. (b) Mean-field energy landscape of a spin-1 sodium condensate plotted as a function of the spinor phase and fractional population in the $m_F = 0$ state. The gray contours represent trajectories of constant energy, while the red separatrix divides running-phase and oscillatory solutions. Microwave dressing modifies the quadratic Zeeman energy and consequently reshapes the energy landscape. 10

3.1 (a) Schematic overview of the complete ultracold sodium experimental apparatus, including the sodium oven assembly, cold plate, differential pumping region, Zeeman slower, MOT coils, bias coils, ion pumps, titanium sublimation pump, and the main experimental chamber. The Zeeman slower consists of positive, negative, and magnetic field reversal sections designed to decelerate the atomic beam before capture in the MOT region. (b) Enlarged view of the magnetic field control system surrounding the science chamber, showing the MOT coils and the three orthogonal pairs of bias coils used for precise magnetic field compensation and positioning of the trapped atomic cloud. 13

3.2 Longitudinal magnetic field profile along the axis of the Zeeman slower used in our laboratory. The magnetic field is produced by a tapered solenoid, yielding the required spatial variation for velocity compensation. Discrete markers indicate experimental measurements obtained using a Hall probe, while the solid curve represents the corresponding numerical simulation. 18

3.3 Schematic illustration of the beam geometry used in the main experimental chamber for laser cooling and imaging of ultracold sodium atoms. Three orthogonal pairs of counter-propagating MOT cooling beams intersect at the center of the chamber to create the magneto-optical trap. Additional repumping beams are overlapped with the cooling beams to maintain atoms within the optical cooling cycle. A separate imaging beam propagates through the chamber for absorption imaging and characterization of the trapped atomic cloud. 20

3.4 Schematic diagram of the homebuilt stabilized bipolar current driver used for the bias coil control system. Low-power transistors Q1 and Q2 are used to isolate the control circuitry from the higher currents flowing through the high-power output transistors Q3 and Q4. The operational amplifier provides proportional-integral (PI) feedback control for rapid and stable current regulation. Additional filtering capacitors and feedback components were incorporated to suppress current noise and improve stability of the magnetic field control system used for MOT positioning and bias field compensation. 22

3.5 Energy level diagram of the sodium D_2 transition showing the laser frequency settings used for cooling, Zeeman slowing, and repumping in the experiment. The main laser system is frequency locked approximately 105 MHz below the $F' = 3$ excited-state level. The MOT cooling beam is detuned by $\delta_c = -7$ MHz from the cycling transition, while the Zeeman slower cooling beam is detuned by approximately -495 MHz to compensate for the large Doppler shifts of the fast atomic beam. Separate repumping beams are used to drive the $F = 1 \rightarrow F' = 2$ transition and return atoms to the cooling cycle. The hyperfine splittings of the excited and ground-state manifolds are also indicated. 24

3.6 Schematic diagram of the laser distribution system used for generating the cooling, repumping, Zeeman slowing, and imaging beams in the experiment. The primary laser source is a frequency-doubled diode laser operating at 589 nm (TA-SHG Pro, 1.2 W). Acousto-optic modulators (AOMs), wave plates, beam splitters, lenses, and polarization optics are used to generate the required frequency detunings and independently control the optical power of each beam. Separate optical paths are used for the MOT cooling beam, Zeeman slower beam, imaging beam, and their corresponding repumping beams. Polarization-maintaining optical fibers transfer the beams from the laser table to the experiment table while preserving beam alignment stability. 26

3.7 Optical layouts used for beam generation, delivery, and imaging in the ultracold sodium atom experiment. (a) and (b) Laser distribution optics on the optical table used for generating the cooling, repumping, slowing, and imaging beams required for MOT operation. (c) Imaging and beam delivery optics near the science chamber used for absorption imaging, beam alignment, and characterization of the ultracold atomic cloud. 27

3.8 Experimental vacuum apparatus and MOT beam used in the ultracold sodium atom experiment. (a) Photograph of the complete experimental setup including the Zeeman slower assembly, segmented cooling structure, MOT region, and main science chamber mounted on the optical table. (b) Fluorescence image of the Sodium MOT observed through the chamber viewport during operation of the MOT. 28

4.1 Physical parameters governing diffraction-limited imaging in a circular lens system. (a) Lens geometry illustrating the focal length (d), lens radius (r), and maximum convergence half-angle (max), which collectively determine the system numerical aperture. (b) Simulated Airy diffraction pattern generated by a circular aperture, shown as a three-dimensional intensity surface and radial cross-sectional profile. The Airy disk radius (R) corresponds to the first intensity minimum, while I/I denotes the normalized intensity distribution in the image plane. 33

4.2 Comparison of the imaging system during the design and implementation stages. (a) Three-dimensional CAD model of the imaging system showing the vacuum chamber, optical rails, imaging optics, optomechanical mounts, and camera assembly used to optimize the optical layout and verify mechanical clearances prior to construction. (b) Photograph of the completed imaging system implemented in the laboratory, showing the assembled optical components mounted on rail systems around the ultrahigh-vacuum chamber for experimental characterization and future absorption imaging of ultracold sodium atoms. 35

4.3 Three-dimensional representation of the optical imaging configuration employed for imaging ultracold sodium atomic clouds. The imaging train comprises achromatic relay lenses, a quarter-wave plate (QWP), a 10× microscope objective, a (589 ± 5) nm bandpass filter, and a CCD camera. Blue solid rays denote the absorption imaging beam, while red dashed rays illustrate fluorescence collection. The optical arrangement forms successive image planes to achieve the required magnification and spatial resolution for diffraction-limited imaging of the atomic cloud. 36

4.4 Three-dimensional optical layout of the dual-view imaging system used for absorption imaging of ultracold sodium atoms. The system consists of independent side- and top-imaging pathways employing relay lenses, quarter-wave plates (QWPs), a polarization beam splitter (PBS), a steering mirror, narrowband 589 nm bandpass filters, and CCD cameras. The optical arrangement enables simultaneous imaging along orthogonal directions while preserving the required magnification and spatial resolution. Yellow arrows indicate magneto-optical trap (MOT) beams and blue arrows denote the absorption imaging beam. 37

5.1 Representative images of the USAF 1951 resolution target acquired using the four imaging configurations investigated in this work: (a) side imaging system at $M = 0.6$, (b) top imaging system at $M = 0.6$, (c) top imaging system at $M = 4$, and (d) side imaging system at $M = 10$. These images were used for magnification calibration, spatial resolution measurements, and intensity profile analysis. . . . 40

5.2 Intensity profiles extracted from selected elements of the USAF 1951 resolution target using the side imaging system at $M = 0.6$. The target elements are arranged in order of increasing spatial frequency from Group 1, Element 3 to Group 6, Element 1. 44

5.3 Intensity profiles extracted from selected elements of the USAF 1951 resolution target using the top imaging system at $M = 0.6$. The target elements are arranged in order of increasing spatial frequency from Group 2, Element 2 to Group 6, Element 1. 44

5.4 Intensity profiles extracted from selected elements of the USAF 1951 resolution target using the top imaging system at $M = 4$. The target elements are arranged in order of increasing spatial frequency from Group 1, Element 3 to Group 6, Element 1. 45

5.5 Intensity profiles extracted from selected elements of the USAF 1951 resolution target using the side imaging system at $M = 10$. The target elements are arranged in order of increasing spatial frequency from Group 5, Element 2 to Group 6, Element 4. 45

List of Tables

4.1 Technical specifications of the PCO Pixelfly CCD camera used for image acquisition. 38

5.1 Measured magnifications of the four imaging configurations. The first uncertainty represents the 95% confidence interval obtained from repeated measurements, while the second uncertainty was calculated using first-order Gaussian error propagation. 42

5.2 Comparison of theoretical and experimentally measured spatial resolutions for the four imaging configurations. 48

Abstract

Optical imaging plays a central role in ultracold atom experiments by enabling quantitative measurements of atomic density, temperature, atom number, and condensate dynamics. Achieving high-fidelity absorption imaging requires a well-characterized optical system with accurately calibrated magnification and spatial resolution. In this work, I designed, implemented, and experimentally characterized a dual-view optical imaging platform for future absorption imaging of ultracold sodium atoms. The system consists of two independent three-lens relay imaging systems providing top and side views of the atomic sample. Two low-magnification configurations with nominal magnification 0.6 were developed for imaging the relatively large sodium magneto-optical trap (MOT), while higher-magnification configurations with nominal magnifications of 4 and 10 were designed for Bose–Einstein condensate (BEC) imaging. The work included the integration and optimization of the laser cooling and trapping apparatus, improvements to the magnetic-field control system, and the alignment and calibration of both imaging paths. Characterization using a laser and a USAF 1951 resolution target yielded measured magnifications of 0.653 ± 0.033 and 0.521 ± 0.016 for the side and top MOT imaging systems, with corresponding spatial resolutions of 13.92 μm and 9.84 μm. The BEC imaging systems achieved measured magnifications of 4.094 ± 0.060 (top) and 10.817 ± 0.172 (side), with spatial resolutions of 9.84 μm and 6.20 μm, respectively. These measurements agree well with the theoretical diffraction-limited resolutions of 7.19 μm for the 0.6 and 4 magnification systems and 2.87 μm for the 10 magnification system, with the remaining differences attributed primarily to practical optical aberrations and alignment tolerances. The calibrated dual-view imaging platform provides the spatial resolution and quantitative accuracy required for absorption imaging of ultracold sodium atoms and establishes the experimental foundation for future investigations of sodium magneto-optical traps, Bose–Einstein condensation, and coherent spin dynamics in spinor sodium gases.

Chapter 1

Introduction

Ultracold atomic gases have emerged as one of the most powerful experimental platforms for investigating quantum many-body phenomena, owing to the exceptional level of control that can be achieved over atomic interactions, trapping potentials, and internal quantum states. Advances in laser cooling and evaporative cooling have enabled the production of dilute atomic gases at nanokelvin temperatures, where quantum statistics dominate the system dynamics and phenomena such as Bose–Einstein condensation become experimentally accessible [1, 2]. Beyond serving as model systems for condensed matter physics, ultracold atoms have become versatile platforms for studies of quantum simulation, precision measurement, nonlinear atom optics, and quantum information science because their interactions can be manipulated with remarkable precision while remaining well isolated from environmental decoherence [3].

Among the alkali atoms used in ultracold atom experiments, sodium possesses several characteristics that make it particularly attractive for laser cooling and quantum gas research. Its electronic structure provides strong cycling transitions on the D_2 line, a relatively large natural linewidth, and favorable hyperfine structure that enable efficient magneto-optical trapping and optical pumping. The spectroscopic properties of sodium, including transition frequencies, hyperfine splittings, transition strengths, and saturation intensities, have been accurately characterized and provide the basis for quantitative optical manipulation and absorption imaging [4]. These favorable atomic properties, together with relatively low inelastic collision rates and well-understood collisional behavior, have established sodium as one of the principal atomic species for Bose–Einstein condensation and spinor quantum gas experiments.

Interest in ultracold sodium extends well beyond the production of Bose–Einstein condensates. Within the $F = 1$ hyperfine manifold, spin-dependent interactions permit coherent spin-changing collisions that redistribute population among the Zeeman sublevels while conserving total magnetization. The microscopic mechanisms governing spin-exchange interactions in sodium

were first identified through measurements of spin-relaxation processes in thermal vapors [5]. At ultracold temperatures these same interactions become coherent, allowing the atomic spin degrees of freedom to evolve collectively according to the spinor Bose–Einstein condensate Hamiltonian [6]. Such systems provide an experimental realization of nonlinear matter-wave optics, where spin populations evolve through coherent spin mixing in direct analogy with nonlinear optical wave-mixing processes. As a result, sodium spinor condensates have become an important platform for investigating quantum magnetism, spin squeezing, entanglement generation, and non-equilibrium many-body dynamics [7].

The realization of these experiments depends critically on the ability to accurately characterize the atomic sample. Optical imaging provides the primary experimental observable from which atom number, cloud dimensions, optical density, temperature, condensate fraction, and spin populations are extracted. In particular, resonant absorption imaging on the sodium D_2 transition has become the standard diagnostic technique because it enables quantitative measurements of atomic density with high spatial resolution. The accuracy of these measurements depends not only on the optical quality of the imaging system but also on careful calibration of its magnification, spatial resolution, and mechanical stability. Residual optical aberrations, imperfect alignment, detector sampling, and mechanical vibrations introduce systematic uncertainties that directly affect the quantitative interpretation of experimental data. Consequently, the imaging system represents one of the most critical components of any ultracold atom apparatus.

The development of a reliable imaging system is particularly important for future studies of spinor Bose–Einstein condensates. Experiments investigating coherent spin dynamics frequently require the detection of small differences in spin populations together with precise measurements of spatial density distributions. State-selective absorption imaging, often combined with Stern–Gerlach separation following time-of-flight expansion, enables direct observation of spin-domain formation, population transfer, and coherent spin evolution. These measurements demand an imaging system that is both optically well corrected and mechanically stable, ensuring that measured density variations originate from the atomic sample rather than imaging artifacts.

The objective of this thesis is to develop and experimentally characterize an optical imaging system for future absorption imaging of ultracold sodium atoms. This work includes the integration of the imaging optics with the existing laser cooling and trapping apparatus, improvements to the magnetic-field control electronics, and quantitative characterization of the optical performance through measurements of magnification and spatial resolution. The imaging system was designed using paraxial optical theory and implemented using a three-lens relay configuration optimized

for the experimental geometry. Its performance was evaluated experimentally using a yellow laser and a USAF 1951 resolution target to establish quantitative calibration of the magnification and imaging resolution prior to experiments with trapped atoms.

The remainder of this thesis is organized as follows. Chapter 2 reviews the theoretical background of laser cooling, magneto-optical trapping, sodium atomic structure, optical imaging, and diffraction-limited resolution. Chapter 3 describes the experimental apparatus, including the vacuum system, laser system, magnetic-field control electronics, and optical layout of the sodium experiment. Chapter 4 presents the design, implementation, and alignment of the imaging system together with the mechanical integration of the optical components into the existing laser-cooling set up. Chapter 5 presents the experimental characterization of the imaging system through measurements of magnification, spatial resolution, and uncertainty analysis. Finally, Chapter 6 discusses the performance of the imaging system, summarizes the principal contributions of this work, and outlines future applications toward quantitative imaging of sodium magneto-optical traps and spinor Bose–Einstein condensates.

Chapter 2

Background and Theoretical Framework

2.1 Laser Cooling, Trapping, and Sodium MOT

A key component of contemporary atomic physics experiments is the capacity to cool and confine diluted gases of atoms to microkelvin and nanokelvin temperatures. The momentum exchange between resonant photons and atoms is exploited by laser cooling. An atom receives a momentum kick proportional to $\hbar k$ in the direction of propagation when it absorbs a photon. When the scattering force is set up to oppose the atomic motion, spontaneous emission randomizes recoil momentum and results in a net velocity damping. Red detuning in Doppler cooling ensure that atoms interact with photons preferentially as they approach the laser, creating a viscous damping force. The Doppler temperature, the lowest temperature that this model predicts, establishes a significant lower limit on the cloud's potential kinetic energy and typically on the order of 100 μK [8].

On the other hand, cooling mechanisms beyond the Doppler limit are observed in alkali atoms with degenerate magnetic sublevels. In multi-level systems, processes such as Sisyphus cooling and polarization gradient cooling take advantage of spatially varying light shifts. Because sodium's ground state hyperfine structure permits a strong coupling between optical pumping and spatial polarization patterns, these sub-Doppler mechanisms work especially well in sodium. The forces pertinent to cooling on the $3^2S_{1/2}$ to $3^2P_{3/2}$ transition are quantitatively described by experimental measurements of scattering cross sections and decay rates, such as those tabulated for the D line manifold. By lowering the sample temperature to the tens of microkelvin regime, these mechanisms work in a magneto optical trap.

The magneto optical trap (MOT) creates a restoring force that confines atoms close to the trap center by combining Doppler cooling and spatially dependent Zeeman shifts (see Figure 2-1). A position-dependent detuning is produced by the interaction of circularly polarized

counterpropagating laser beams with an applied magnetic field gradient. Photons from the beam are preferentially scattered by atoms that are displaced from the trap center, pushing them back toward the center.

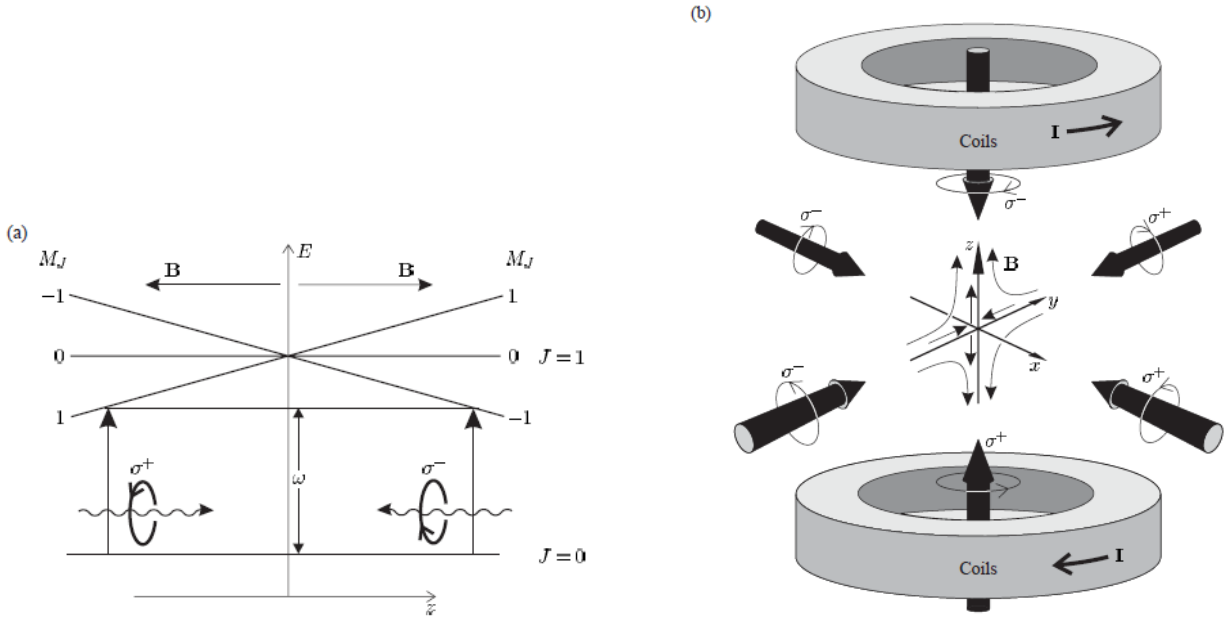

(a) (b)

Figure 2.1: (a) Schematic representation of spatially varying Zeeman energy shifts, illustrating position-dependent resonance conditions and the preferential absorption of oppositely circularly polarized light across the trapping region. (b) Schematic illustration of a magneto-optical trap (MOT) consisting of six counter-propagating laser beams and a pair of coils in an anti-Helmholtz configuration, generating a quadrupole magnetic field with a zero-field point at the trap center.

Because of the favorable Clebsch–Gordan coefficients that arises when cooling the $F = 2$ ground manifold to the $F' = 3$ excited state, the D_2 cycling transition in sodium allows for efficient laser cooling. Atom numbers greater on the order of a few billion are regularly produced by the MOT, which is adequate for subsequent experiments like precision imaging or evaporative cooling [9].

2.2 Optical System Design for High Precision Imaging

An optical system that maps the object plane to the camera with minimal distortion, stable magnification, and low aberration is necessary for accurate imaging of ultracold sodium clouds. Gaussian beam propagation and lens conjugation relationships are used in the design of these systems. In order to attain the desired magnification while keeping an adequate numerical aperture, a two-lens telescope is frequently used. Since imaging depends on comparing absorbed and unabsorbed intensities, the relay optics must accurately maintain the spatial phase and intensity distribution of the probe beam over time [10].

Spherical distortion, astigmatism, and coma are examples of aberrations that reduce image fidelity and must be reduced by carefully selecting and positioning lenses. Systematic variations in the imaging path are introduced by temperature changes and mechanical drift. As a result, athermal design principles and stiff mounting structures are crucial. The image scale or focus can be impacted by even sub-micron changes in camera or lens position, especially when high resolution measurements are needed. The final measurement accuracy is determined by the engineering of the optical layout since absorption images encode the optical depth of the cloud across micrometer-scale features [10]. A stable, high-resolution imaging device that can support quantitative studies of ultracold sodium is built using the design principles mentioned above.

2.3 Absorption Imaging Theory and Measurement Accuracy

Absorption imaging is use to determine the column density of the atomic cloud. A probe beam close to resonance is passed through the cloud. Atoms absorb photons from the probe beam in accordance with the Beer–Lambert law. The absorption signal is directly proportional to the column density and the resonant cross-section. In the case of sodium atoms, the cross-section is very sensitive to detuning values, the saturation intensity, and the particular transition. It is important to check that the probe field is in the linear range by keeping the intensity well below the saturation intensity [11].

For the imaging process, it is necessary to have two reference images: one image with the atoms and one image with the probe field alone. The ratio of the two provides an image with a spatial distribution of optical density. Systematic errors arises from interference patterns, etalon effects, and inhomogeneities in the probe field. Furthermore, off-resonant scattering and polarization can affect the scattering rate. The scattering rate and the matrix elements, as contained in the data tables for sodium (found in [4]), are important for the determination of the correct cross-section value at the resonant energy [4]. At high resolution, all the above factors affect the precision with which the density or the dynamics can be determined.[12].

2.4 Resolution, Optical Performance Metrics

The resolving power of the imaging system defines the smallest possible structures that can be resolved. The Rayleigh criterion states that two point-like sources can be resolved if they are separated about $0.61\lambda/\mathrm{NA}$ [13]. In the general case, the point spread function (PSF) defines the system's response to a point-like object. The smaller the point spread function, the higher the resolution. The deviations from the ideal system are due to diffraction effects, lens errors,

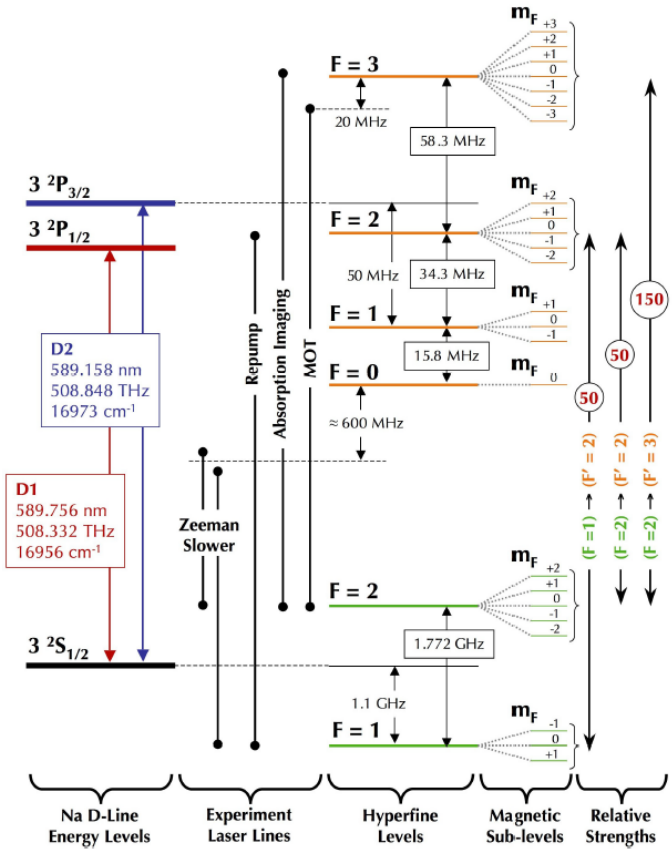

Figure 2.2: Energy level structure of the sodium D_2 transition.

misalignments, and motion blurring.

Aside from the PSF, the modulation transfer function (MTF) is another way of describing the imaging system in the frequency domain. This function defines the contrast with which details of a given frequency are transmitted. When it comes to the application of the system for ultracold sodium, details of interest would be the edges of thermal clouds, micrometer size spin textures, and density modulations caused by the coherent spin dynamics of the system. The sources of noise in the system would be photon shot noise, read noise, and vibrations [14].

The electronic structure of sodium also plays a part in both cooling and imaging. The straight transition is the D_2 transition at 589 nm, which is between the $3^2S_{1/2}$ ground state and the $3^2P_{3/2}$ state [15]. Hyperfine structure results in $F = 1$ and $F = 2$ levels for the ground state. Detailed information about the splittings is required for adjusting both cooling and imaging lasers. In experiments that use state separation or manipulation of the internal spin state, Zeeman shifts due to magnetic fields must be taken into account as well (see Figure 2.2).

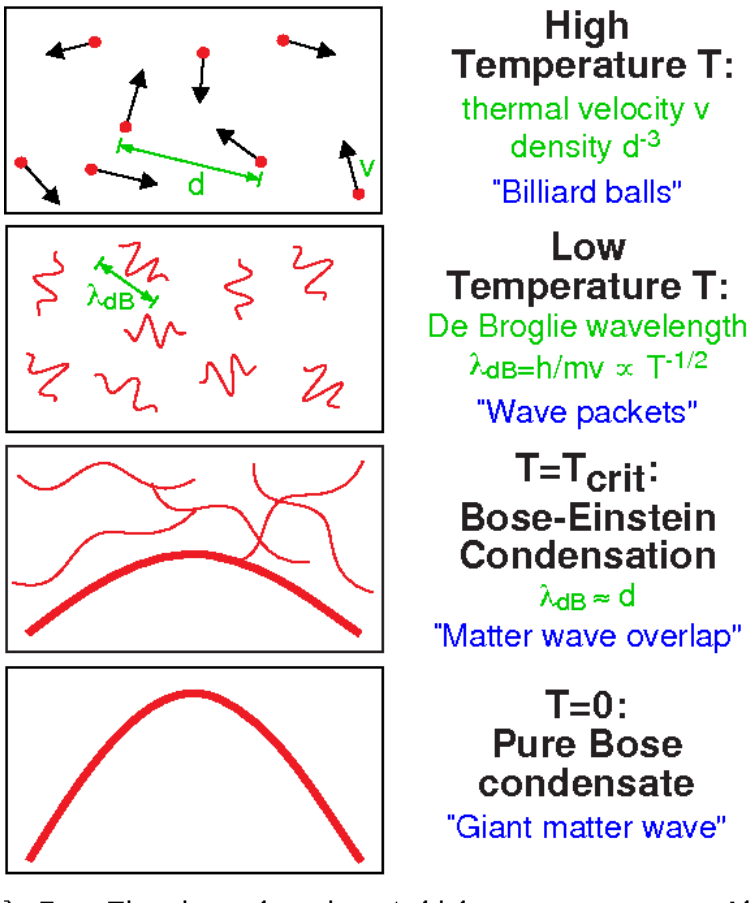

Figure 2.3: Schematic illustration of the criterion for Bose–Einstein condensation.

2.5 Spinor Quantum Gas Theory

Unlike scalar Bose–Einstein condensates, in which all atoms occupy a single internal state, a spinor Bose–Einstein condensate (BEC) retains the atomic spin degree of freedom, allowing atoms to populate multiple magnetic sublevels simultaneously. Consequently, the condensate order parameter becomes a spinor wavefunction whose dynamics are governed by both density-dependent and spin-dependent interactions. This additional internal degree of freedom gives rise to a variety of collective quantum phenomena, including spin textures, spin domains, coherent spin oscillations, quantum phase transitions, and the generation of highly entangled many-body states [7, 16].

The experiments presented in this thesis employ ultracold sodium atoms in the $F = 1$ hyperfine manifold. Sodium is an antiferromagnetic (polar) spinor gas because its spin-dependent interaction coefficient is positive, in contrast to ferromagnetic species such as ^{87}Rb. As a result, sodium exhibits coherent and reversible spin-changing collisions in which two atoms initially occupying the $m_F = 0$ Zeeman state collide and are converted into one atom in the $m_F = +1$ state and one atom in the $m_F = -1$ state while conserving both total spin projection and energy [17, 18]. This process is illustrated schematically in Fig. 2.4.

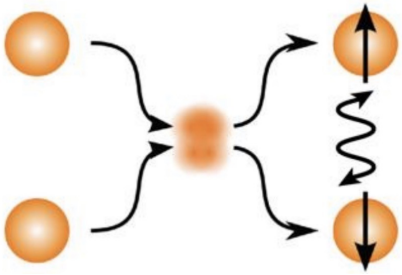

Figure 2.4: Schematic illustration of spin-changing collisions in an $F = 1$ sodium spinor Bose–Einstein condensate. Two atoms initially occupying the $m_F = 0$ state collide through spin-exchange interactions and are converted into correlated atoms in the $m_F = +1$ and $m_F = -1$ states while conserving total magnetization. The process is analogous to optical four-wave mixing and generates quantum correlations between the two output states.

The coherent spin dynamics are described by the spinor Hamiltonian under the single-mode approximation (SMA), in which all spin components are assumed to share the same spatial wavefunction. This approximation is valid when the condensate size is smaller than the spin healing length, suppressing the formation of spin domains [7, 19]. The Hamiltonian can be written as

$$H = \frac{c}{2}\hat{F}^2 - q\hat{a}_0^\dagger \hat{a}_0, \tag{2.1}$$

where c denotes the spin-dependent collisional interaction energy, $\hat{F}$ is the total spin operator, and q is the quadratic Zeeman energy shift. The first term originates from spin-exchange interactions and drives coherent spin mixing, whereas the second term represents the quadratic Zeeman effect, which can be controlled experimentally through external magnetic fields or microwave dressing fields [20, 21]. Since the linear Zeeman shifts of the $m_F = \pm 1$ states are equal and opposite, they cancel for spin-conserving collisions and are therefore neglected.

Expanding the interaction Hamiltonian reveals the spin-exchange terms responsible for coherent population transfer between the Zeeman sublevels. The dominant contribution corresponds to the reversible conversion

$$2m_F = 0 \leftrightarrow m_F = +1 + m_F = -1,$$

which is mathematically equivalent to four-wave mixing in nonlinear optics. This analogy has motivated extensive research into quantum-enhanced atom interferometry, spin squeezing, and entanglement generation using spinor condensates [17, 22, 23, 24].

Within the mean-field approximation, the spin dynamics can be described by two canonical variables: the fractional population in the $m_F = 0$ state, ρ_0, and the relative spinor phase

$$\theta = 2\theta_0 - \theta_{+1} - \theta_{-1}, \tag{2.2}$$

where θ_i represents the quantum mechanical phase of the corresponding Zeeman component. For a condensate with zero longitudinal magnetization, the corresponding mean-field energy functional becomes [19]

$$E = q(1-\rho_0) + c\rho_0 \left[(1-\rho_0) + \sqrt{(1-\rho_0)^2}\cos\theta\right]. \tag{2.3}$$

The resulting energy landscape is shown in Fig. 2.5. The contours define trajectories of constant energy, analogous to the motion of a non-rigid quantum pendulum. Depending on the initial state, the condensate follows either oscillatory (bounded) trajectories or continuously evolving (running-phase) trajectories, which are separated by a dynamical separatrix. The location of the separatrix can be tuned by adjusting the quadratic Zeeman shift through microwave dressing, thereby providing precise experimental control over the spin dynamics [19, 25, 20].

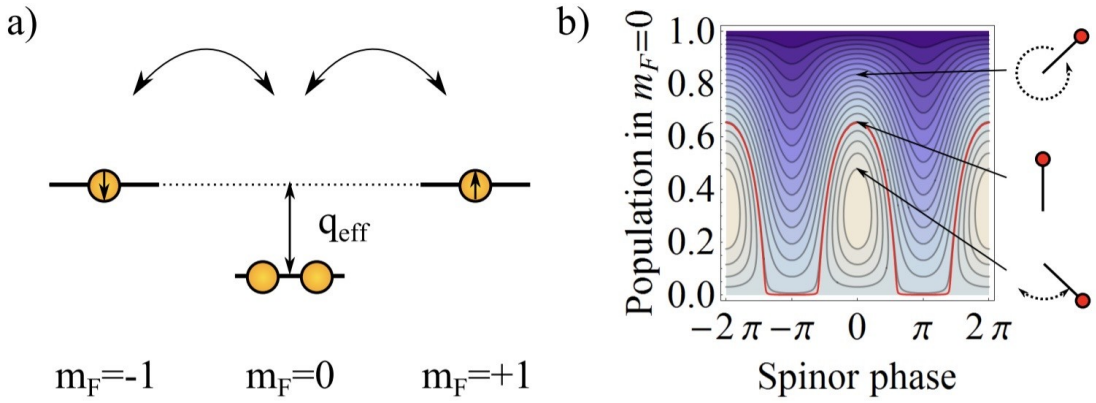

Figure 2.5: (a) Spin-changing collisions in an $F = 1$ sodium spinor condensate driven by spin-exchange interactions. (b) Mean-field energy landscape of a spin-1 sodium condensate plotted as a function of the spinor phase and fractional population in the $m_F = 0$ state. The gray contours represent trajectories of constant energy, while the red separatrix divides running-phase and oscillatory solutions. Microwave dressing modifies the quadratic Zeeman energy and consequently reshapes the energy landscape.

These coherent spin dynamics evolve through changes in both the spatial density distribution and the populations of the individual Zeeman states. Observation of spin oscillations, domain formation, and population transfer therefore requires an imaging system capable of resolving

micrometer-scale features with high spatial resolution and sufficient signal-to-noise ratio. The imaging system developed in this work provides the optical performance necessary for quantitative studies of spinor condensate dynamics and forms the experimental foundation for future investigations of microwave-controlled spin mixing and quantum many-body phenomena.

Chapter 3

Experimental Set Up for Cooling and Trapping

3.1 Introduction

To realize ultracold atomic systems in the laboratory, one must have a very controlled environment where one can manipulate neutral atoms with a high degree of precision. The creation and investigation of Bose–Einstein condensates (BECs) require advanced experimental facilities, such as ultra-high vacuum systems, stable magnetic field generation, laser cooling systems, and precise optical control. Sodium atoms are particularly well suited for such experiments, owing to their favourable optical transitions, well characterised atomic structure, and strong collisional properties, and are an important platform for the study of spin dynamics, matter-wave optics and quantum many-body phenomena.

The preparation of ultracold sodium gases can be broken down into a number of sequential steps, starting with the generation of an atomic beam from a heated oven source, followed by longitudinal cooling via a Zeeman slower and finally, the capture of the atoms in a magneto-optical trap (MOT). Evaporative cooling is then used to reach the nano-kelvin temperatures for quantum degeneracy and Bose-Einstein condensation. All subsystems of the apparatus should be stable and operated in a timing sequence to allow efficient loading of atoms, to minimize heating effects, and to achieve long trap lifetimes.

The entire experimental apparatus designed for the laser-cooling and trapping of Sodium. The system includes an ultra-high vacuum assembly, sodium oven, Zeeman slower, experimental chamber, magnetic field control hardware and laser distribution network. Special emphasis is placed on the design of the magnetic field control circuit and noise reduction methods used for stable operation of the bias coils. The laser setup, light distribution, acousto-optic modulators (AOMs) and optical shutter systems are also explained in detail. These are combined to create the experimental platform for studying the dynamics of spins in ultracold gases of sodium.

3.2 Overview of the Experimental Apparatus

This section gives a general description of the experimental apparatus developed for the production and trapping of ultracold sodium atoms. The apparatus was designed to obtain ultra-high vacuum conditions in the main experimental chamber with a pressure less than 10^{-10} Torr. This is because the low pressures are necessary to reduce the loss of atoms and unwanted heating due to collisions between trapped sodium atoms and hot background gas particles. A low enough background pressure will greatly increase the lifetime of the trapped atomic cloud and increase the overall efficiency of the laser cooling process.

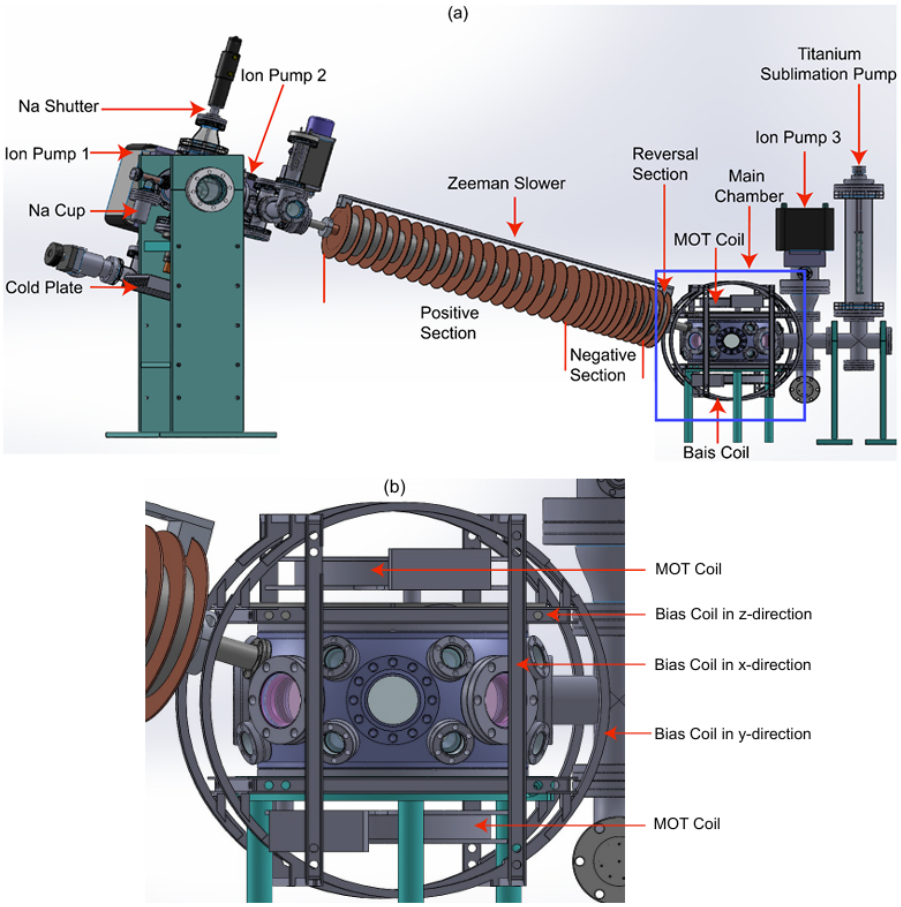

Figure 3.1: (a) Schematic overview of the complete ultracold sodium experimental apparatus, including the sodium oven assembly, cold plate, differential pumping region, Zeeman slower, MOT coils, bias coils, ion pumps, titanium sublimation pump, and the main experimental chamber. The Zeeman slower consists of positive, negative, and magnetic field reversal sections designed to decelerate the atomic beam before capture in the MOT region. (b) Enlarged view of the magnetic field control system surrounding the science chamber, showing the MOT coils and the three orthogonal pairs of bias coils used for precise magnetic field compensation and positioning of the trapped atomic cloud.

The experimental system is composed of multiple separate subsystems, such as the vacuum assembly, sodium oven source, Zeeman slower, main science chamber, magnetic field control

hardware, and optical distribution setup. The sodium atoms are first created in a heated oven and then ejected as a thermal atomic beam. These atoms' velocities are too high to be directly captured in a magneto-optical trap, so a Zeeman slower is used to slow the atoms' longitudinal velocity by radiation pressure from a laser beam that moves against them and a spatially varying magnetic field. The slowed atoms are then injected into the main experimental chamber where they are trapped and cooled with a six-beam MOT configuration.

Special emphasis was placed on the optimization of the operating conditions of the sodium oven and Zeeman slower to achieve as high an atom loading efficiency as possible, while maintaining stable vacuum conditions. The oven temperature was carefully controlled to achieve a large enough atom flux of sodium without adding too much background pressure to the vacuum system. Likewise, the current values were optimized for each section of the Zeeman slower to produce the desired magnetic field profile for efficient deceleration of the atomic beam.

Precise magnetic field control is another important aspect of the experimental apparatus. The MOT coils create magnetic field gradients for trapping atoms and extra bias coils correct for stray magnetic fields and enable precise tuning of the magnetic field in the vicinity of the experimental chamber center. To reduce the fluctuations of the magnetic field, stable and low-noise current control circuits were designed to obtain the near zero residual magnetic field at the trapping region. This level of control is especially critical for future experiments with coherent atomic dynamics and spin manipulation, as well as for stable cooling conditions.

The following subsections provide a detailed description of the various components of the experimental setup: Vacuum system, oven assembly, Zeeman slower, experimental chamber, magnetic field control system, and laser infrastructure used throughout the experiment.

3.2.1 Ultra-High Vacuum Assembly

The experiment of ultracold sodium atoms is conducted in an ultra-high vacuum (UHV) apparatus, which is mainly made of stainless steel. The main science chamber is a stainless steel ultra-high vacuum chamber (UHVC, Kimball Physics, 8" extended spherical octagon) that is the central part of the apparatus for laser cooling, trapping and imaging the atomic cloud. It is essential to keep the pressure inside the experimental chamber very low to obtain long trap lifetimes and efficient laser cooling performance. The pressure in the main chamber is kept below 10^{-10} Torr in the present configuration to reduce the number of collisions between the trapped sodium atoms and energetic background gas particles. These collisions may result in loss of atoms, heating of the trapped cloud and decrease in the number of atoms that can be trapped in the

magneto-optical trap.

Pressures of 10^{-10} Torr are difficult to attain, especially since the sodium oven is at a high temperature and is continuously emitting sodium vapor into the vacuum system. The pressure in the oven region is usually about 10^{-8} Torr, much higher than the pressure in the science chamber. A differential pumping stage is placed between the high pressure oven and the trapping region to separate the two regions. The intermediate section offers a higher pressure gradient along the atomic beam path and significantly lowers the gas flow into the science chamber.

The differential pumping chamber is joined to the oven assembly by a narrow custom fabricated stainless steel tube, 5" long and 0.3" in diameter, welded to a double sided CF flange. A tube of similar design is used to link the differential pumping section with the Zeeman slower. These narrow tubes offer some conductance reduction to keep the different pressure regions separate in the apparatus while still providing efficient transport of the sodium atomic beam from the oven to the trapping chamber.

Multiple ion pumps are placed at various points of the apparatus and pumping is carried out continuously throughout the vacuum system. The system consists of four 50 l/s ion pumps (Duniway DSP-OSO-5125-M). The first ion pump is located in the vicinity of the oven region, the second is mounted on the differential pumping chamber, and the third and fourth is directly mounted on the main experimental chamber. The approximate pressures in the oven section, the differential pumping section and the science chamber are 10^{-8} Torr, 10^{-9} Torr and $< 10^{-10}$ Torr, respectively. This staged pressure reduction is crucial to maintain the low background collision environment required for trapping experiments with ultracold atoms.

The vacuum system also includes a titanium sublimation pump that is attached to the main chamber. When the sublimation pump is turned on, the filament is heated for 20 minutes, and the titanium is deposited on any nearby metallic surfaces inside the chamber. The newly deposited titanium layer serves as an efficient getter material that chemically binds residual gas molecules that are present in the vacuum system, thus further enhancing the attainable vacuum quality.

The oven-side ion pump is equipped with an angle valve to allow for rough pumping and maintenance of the vacuum. This valve can be used to connect the vacuum system to a portable pumping station with a turbo-molecular pump and a mechanical backing pump (Pfeiffer HiCube 80 Eco). The rough pumping system is employed when the pump is first being pumped down or when maintenance is being performed. Also, the angle valve allows for a controlled backfill of the vacuum system with dry N2 gas when venting of the apparatus is required.

3.2.2 Thermal Sodium Source

The sodium atomic beam is produced in a stainless steel oven assembly that is located at the end of the vacuum apparatus. The main function of the oven is to produce a large and stable flow of thermal sodium atoms for the following slowing and trapping processes. The sodium reservoir is heated to about 345 °C, to achieve the needed atomic flux. At this temperature, the sodium atoms have sufficient vapor pressure to create a powerful effusive atomic beam that is directed towards the Zeeman slower and the main experimental chamber.

The oven reservoir is a 2.75" Conflat stainless steel cup filled with a prescored 5 g sodium ampule (Strem Chemicals 93-1020.5). The ampule is broken under atmosphere just before it is installed in the oven assembly, and just a few minutes before the vacuum pumping is started. This process reduces the amount of time that sodium is exposed to air and makes loading easier.

The oven includes a custom-made copper oven nozzle attached to the reservoir, which is used to generate a collimated atomic beam. The nozzle is 1.7 inches long and 0.7 inches in diameter, but 0.24 inches in inner diameter. A high thermal conductivity was chosen for copper due to its uniform heating throughout the nozzle structure. The front and back parts of the nozzle are heated to about 415 °C, to avoid condensation and deposition of sodium atoms in the nozzle tube. The higher the nozzle temperature is kept above the reservoir temperature, the more continuous the atomic flow and the less the nozzle clogs, which causes the intensity of the beam to decrease over time.

The nozzle geometry was designed so that the ratio of thermal volume to surface area is as high as possible, which minimizes radiative heat loss under vacuum conditions, and the nozzle walls are relatively thick. Commercial PID temperature controllers (Automation Direct S4848-CR and Avatar CIP-12-20) are used in conjunction with flange mounted heaters (Tempco MPP51101, MPP02838, MPP52501) to provide stable thermal operation of both the oven reservoir and nozzle. The operating temperatures are actively controlled and thermal stability is achieved over long periods of time during experimental operation.

Over the course of months, sodium will deposit on the viewport of the oven and on the 1.33" CF viewport which is opposite the Zeeman slower beam path in the main chamber. This deposition causes a decrease in optical transmission and has a negative impact on the Zeeman slowing process because the slowing laser is passing through this viewport. The lower the optical transmission, the less efficient the atomic slowing, which results in lower loading rates and numbers of atoms trapped in the MOT. Furthermore, sodium on the oven viewport makes it more difficult to see

the nozzle opening during regular diagnostics.

In order to prevent sodium deposition on the contaminated windows without venting the vacuum system, the contaminated windows are illuminated with UV light using LED sources (LED Engin LZ1-UV00-0000 1.2W LED @ 365mm). The UV exposure promotes the desorption of sodium atoms from the surfaces of the windows, and contributes to the restoration of the optical transparency. This is a beneficial process because it can be done in place without compromising the vacuum integrity of the oven and the main chamber, and without altering the low pressure inside the main chamber.

To further minimise sodium background pressure a custom designed copper cold plate is fitted within the oven chamber. The cold plate is thermally coupled to the atmosphere side by means of a thick copper feedthrough and is cooled to a temperature of $-12\,^{\circ}\mathrm{C}$ by a water-cooled thermoelectric cooling assembly of TEC elements (6* TEC1-12706). The cold plate collects the sodium atoms emitted at larger divergence angles from the nozzle and does not add much to the background vapour pressure within the oven region.

A 0.25" diameter circular aperture is placed at the center of the cold plate so that only the central part of the atomic beam can pass through to the differential pumping tube and then into the Zeeman slower. This configuration not only collimates the beam, but also minimizes the amount of unwanted sodium vapor in the chamber. Also, a pneumatic shutter is placed behind the cold plate that allows for complete mechanical switching of the atomic beam in the various steps of the experimental sequence.

3.2.3 Zeeman Slower

The experiment is operated in two steps: a Zeeman slower is used for the initial laser deceleration of Sodium atoms. The thermal velocities of the sodium atoms leaving the oven are in the hundreds of meters per second, much higher than the capture velocity of the magneto-optical trap. The longitudinal velocity of the atomic beam needs to be reduced first in order to efficiently load atoms into the MOT. This deceleration is accomplished through the use of a counter-propagating laser beam and a spatially varying magnetic field created by the Zeeman slower assembly.

The slowing beam is red-detuned by a few hundred MHz from the sodium cooling transition. Atoms approaching the MOT region absorb photons from the counter-propagating laser beam, and are subject to a radiation pressure force in the opposite direction. Spontaneous emission and continuous absorption decrease the kinetic energy of the atoms and slowly slow the atomic beam.

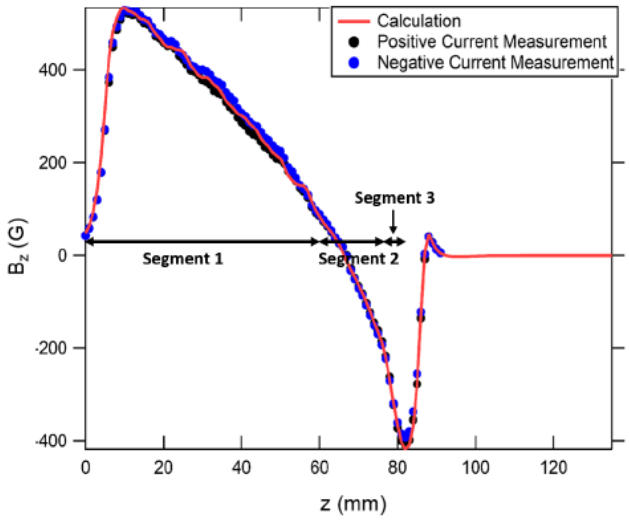

Figure 3.2: Longitudinal magnetic field profile along the axis of the Zeeman slower used in our laboratory. The magnetic field is produced by a tapered solenoid, yielding the required spatial variation for velocity compensation. Discrete markers indicate experimental measurements obtained using a Hall probe, while the solid curve represents the corresponding numerical simulation.

As the atoms slow down, however, the Doppler shift of the atoms will vary continuously, and the atoms will no longer be in resonance with the slower laser. To counteract this changing Doppler shift, the Zeeman slower magnets creates a spatially varying magnetic field which results in a spatially varying Zeeman shift along the slowing direction.

The magnetic field profile of the slower is controlled by three independently adjustable power supplies (Extech DCP60). These are computer-controlled supplies that control the current to various parts of the Zeeman slower coil assembly and are called segment 1, segment 2 and segment 3. The positive field section of the slower is controlled by the segment 1, the negative field section of the slower is controlled by the segment 2, and the magnetic field reversal region is controlled by the segment 3, as shown previously in Fig. 3.2 and Fig. 3.1(a). The magnetic field profile can be fine adjusted and the slowing efficiency optimized during experimental operation, because of the independent control of these segments.

The Zeeman slower coil is a tapered solenoid wrapped around the atomic beam tube. The solenoid is split into 30 sections to increase thermal stability and avoid over-heating during operation. The building is filled with copper discs between the adjacent sections to improve passive heat dissipation across the building. The segmented design provides better thermal uniformity and helps to maintain the stable operation conditions during long experimental runs.

The spatially varying magnetic field created by the tapered solenoid causes a position-dependent

Zeeman shift which continuously compensates the Doppler shift of the decelerating sodium atoms (see Figure 3.2). The atoms are thus kept close to resonance with the slowing laser for most of the slowing trajectory, which is why the laser is called "slowing". In the present experiment, the velocity of the sodium atoms was slowed down from about 700 m/s to almost 20 m/s, within the range of the capture velocity of the magneto-optical trap, using a Zeeman slower. The efficient operation of the Zeeman slower is thus essential to maximize MOT loading rates and obtain large numbers of trapped atoms in the experimental chamber.

3.2.4 Main Experimental Chamber

The main science chamber is made of stainless steel and is the central chamber for laser cooling, trapping, imaging and future coherent manipulation of the ultracold sodium atoms. The chamber was designed to allow for large optical access, multiple electrical feedthroughs, and flexibility for integration of magnetic coils, imaging systems, and microwave components needed for advanced experiments with ultracold atoms.

There are eight 2.75" CF viewports symmetrically placed around the trapping region in the chamber. Four of these viewports are used mainly for cooling and repumping of the laser beams which cross at the centre of the chamber to create the magneto-optical trap. Two other 2.75" viewports are used for side imaging of the atomic cloud. The optical access of these ports allows for the characterization of the trapped atoms and monitoring the cooling process during various stages of the experiment by using absorption and fluorescence imaging systems.

The chamber features sixteen 1.33" CF ports throughout the chamber, as well as the larger viewports. Two of these smaller ports are along the axis of the atomic beam and are used for the incoming atomic beam from the Zeeman slower and for the Zeeman slowing laser beam that travels in the opposite direction. This alignment enables the efficient transfer of slowed sodium atoms to the centre of the chamber, where they are trapped.

One of the 1.33" CF ports is also used for electrical feedthrough to a custom built antennas inside the vacuum chamber. The antenna is a loop RF antenna which works at the frequency range from 50 kHz to 1 MHz. This antenna is used to excite the transitions between the magnetic sub-levels of the Zeeman-split $F = 1$ hyperfine manifold. These transitions are relevant to future experiments with coherent spin manipulation and preparation of the spin state of ultracold sodium atoms.

A second antenna,located below the chamber, is a home-built Yagi antenna, for frequencies of

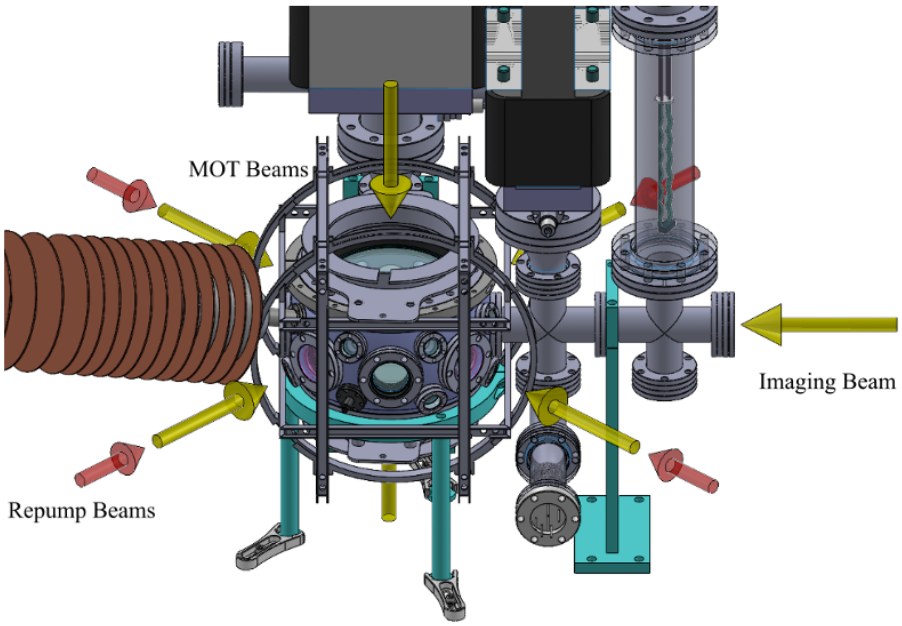

Figure 3.3: Schematic illustration of the beam geometry used in the main experimental chamber for laser cooling and imaging of ultracold sodium atoms. Three orthogonal pairs of counter-propagating MOT cooling beams intersect at the center of the chamber to create the magneto-optical trap. Additional repumping beams are overlapped with the cooling beams to maintain atoms within the optical cooling cycle. A separate imaging beam propagates through the chamber for absorption imaging and characterization of the trapped atomic cloud.

about 1.8 GHz. This antenna is used to excite transitions between the two hyperfine ground-state manifolds for the $F = 1 \rightarrow F = 2$ transition. Control of these hyperfine states by microwave fields is crucial for our studies of spinor dynamics, microwave dressing and coherent population transfer techniques.

Two large 8" CF viewports are also located along the vertical axis of the chamber. The large optical windows are used for the vertical pair of MOT beams and for the imaging of the trapped atomic cloud from above. The large aperture size provides excellent optical access, and enables the use of wide laser beams and high numerical aperture imaging configurations. The different viewports and feedthroughs combine to provide a versatile platform for laser cooling, imaging, radio-frequency manipulation and future Bose–Einstein condensation experiments.

3.2.5 Magnetic Field Control System

The generation and stabilization of magnetic field is an integral part of the magneto-optical trapping system. The formation of a stable MOT also requires a well controlled magnetic field gradient, centered within the experimental chamber, besides the cooling laser beams. In the present section, the focus will be on the magnetic field control infrastructure that has been implemented in the experiment, whereas in Section 3.3 the optical system used for laser cooling

will be discussed.

The ability to control the magnetic field accurately is not only essential for the efficient operation of the MOT but also for future experiments in which the dynamics of spinor gases and coherent spin-changing collisions of ultracold sodium gases will be investigated. These systems are characterized by strong quadratic Zeeman effect, which changes the relative energies of atomic spin states, and strongly influences the collision dynamics. The quadratic Zeeman shift of sodium is of order $\sim$ 700 Hz/G^2, while the characteristic collision energy scale is of order $\sim$ 30 Hz. Therefore, any changes in the magnetic field, no matter how small, can have a strong effect on the dynamics of the spins and coherent evolution in the atomic cloud. A magnetic field of about 100 mG is needed to be controlled in the spatial area where the ultracold atoms are present, to guarantee stable experimental conditions.

3.2.5.1 MOT Coil Assembly

The quadrupole magnetic field used for magneto-optical trapping is achieved by a pair of anti-Helmholtz coils, located above and below the experimental chamber along the vertical (z) axis, as illustrated in figure (Fig. 3.1(b)). These coils, also known as the MOT coils, create a magnetic field gradient that has a zero crossing at the center of the chamber, allowing the sodium atoms to be trapped and cooled simultaneously.

The diameter of each MOT coil is 140 mm and the thickness is 178 mm. Insulated copper tube (outer diameter 3.18 mm and inner diameter 1.8 mm) is used as the winding material. During high current operation, the hollow copper tubing enables water to flow through the coils for efficient thermal management. The coils can safely operate with currents up to 82 A, due to the maintenance of the cooling water temperature near 30 °C and the total number of turns of copper tubing (20 turns).

With these operating conditions, the MOT coils produce a maximum magnetic field gradient of 12 G/cm at the center of the experimental chamber. This gradient is enough to create a well compressed and stable magneto-optical trap, where the atoms are well trapped and the loading rate is high.

3.2.5.2 Bias Coil Configuration

Auxiliary magnetic fields are also needed to cancel out stray magnetic fields in the environment, which are present near the experimental chamber, in addition to the quadrupole trapping field. The magnetic field of the Earth and nearby ion pump magnets can cause the center of the

MOT to shift and can introduce asymmetries in the trapping potential. Three sets of separate Helmholtz bias coils are placed around the chamber to compensate for these effects and keep the magnetic field in the trapping region near zero.

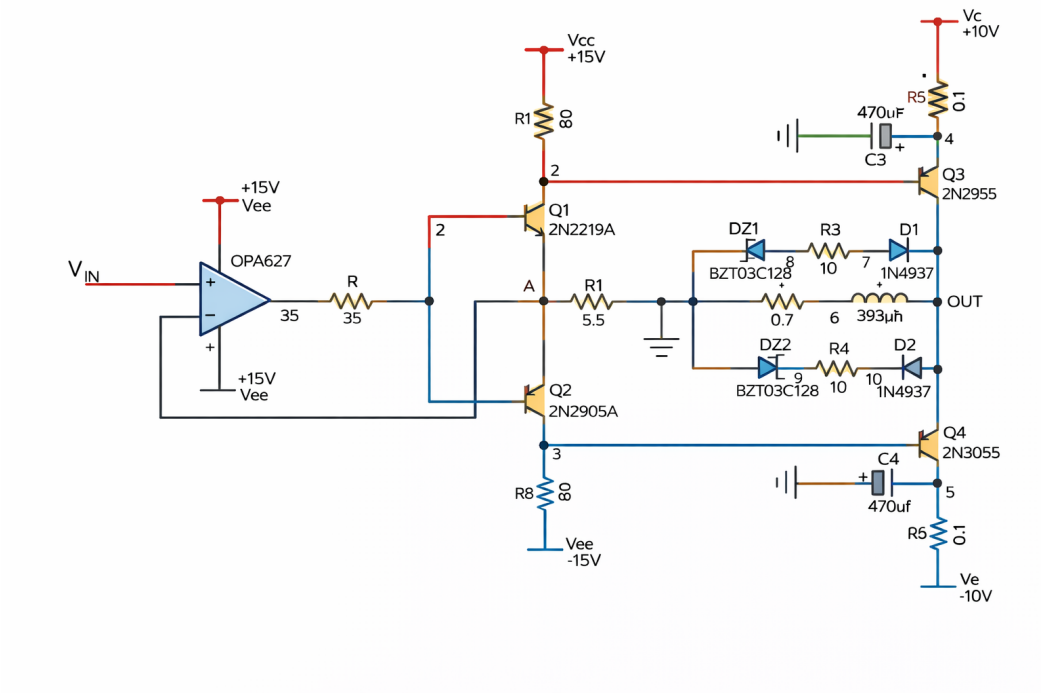

Figure 3.4: Schematic diagram of the homebuilt stabilized bipolar current driver used for the bias coil control system. Low-power transistors Q1 and Q2 are used to isolate the control circuitry from the higher currents flowing through the high-power output transistors Q3 and Q4. The operational amplifier provides proportional-integral (PI) feedback control for rapid and stable current regulation. Additional filtering capacitors and feedback components were incorporated to suppress current noise and improve stability of the magnetic field control system used for MOT positioning and bias field compensation.

These bias coils allow a fine control of the magnetic field in the three orthogonal spatial directions and enable a precise positioning of the trapped atomic cloud. The MOT can be centered accurately and kept at a stable position when the Zeeman slower magnetic field is turned on or off during experimental operation by adjusting the coil currents.

The geometry of each bias coil pair is different, depending on the space available around the chamber, as shown in Fig. 3.1(b). The bias coils along the z-direction are square coils with side lengths of 235.5 mm, and generate a magnetic field of about 3 G at the center of the chamber at 5 A. The coils along the x-direction are also square in geometry with side length of 275 mm, and produce a field of 5 G at 5 A. The bias coils along the y-direction are circular, 294 mm in diameter, and are also capable of producing a field of 5 G at 5 A.

All bias coils are made of 33 turns of copper wire and are rated for a current range of ± 5 A. The supporting coil frames were made with a 3D printer at the machine shop, which enabled quick

customization and mechanical alignment around the vacuum chamber.

3.2.5.3 Bias Coil Current Stabilization

Custom bipolar current supplies and amplifiers were designed in-house for the stable and quickly adjustable magnetic fields of the bias coils. The supplies can provide controlled currents of ± 5 A to each of the six bias coils. The schematic diagram of the control electronics is shown in Fig. 3.2 and the assembled hardware is presented in Fig. 3.3.

Proportional-integral (PI) feedback control circuits were incorporated into each supply to effect current switching at a high rate. However, large fluctuations and oscillations in the output current signals were initially seen, leading to higher magnetic field noise in the vicinity of the trapping region. This noise made the MOT unstable and caused less precise magnetic field compensation.

Some modifications have been made to make the current control system more stable. To reduce the high frequency noise and fluctuations in the output signal, a 23 μF filtering capacitor was placed in parallel with the output of each current supply. Furthermore, a 10 nF capacitor was placed in the PI feedback path to change the gain characteristics and to enhance the overall stability of the loop, as shown in Fig. 3.3.

The proportional and integral gain potentiometers were then adjusted by trial and error for each supply for further optimization. These changes eliminated oscillatory behavior throughout the operating current range and greatly enhanced the signal-to-noise ratio of the coil currents. The filtering modifications did stabilize the output current of the supplies, but did make the switching time of the supplies about 1.5 ms, which is much longer than the original design specification of around 10 μs. The increased stability and decreased magnetic noise, however, were seen to be much more advantageous for reliable operation of ultracold atoms and spin sensitive experiments, even though the response is slower.

3.3 Laser System Setup

The laser infrastructure must be very stable and well controlled, in addition to the ultra-high vacuum environment and magnetic field control system, to enable laser cooling and trapping of sodium atoms. All cooling, repumping, slowing and imaging beams required for preparation and characterization of the ultracold atomic cloud are generated by the laser system used in the experiment. This section explains the optical setup which was used throughout the experiment, such as the laser source, the frequency stabilization method, the beam distribution system, the

acousto-optic modulators, and the mechanical shutter configuration.

3.3.1 Laser Beam Distribution

The main laser source used in the experiment is a frequency-doubled diode laser (TOPTICA TA-SHG PRO) with an output power of about $P \approx 1.2$ W, and a wavelength of $\lambda = 589\ nm$. This is the wavelength of the sodium D_2 transition, and is used for all cooling and trapping in the experiment. The laser output is split into two optical paths immediately after the laser output. The first part is aimed at a saturated absorption spectroscopy system for active frequency stabilization of the laser. The second portion is utilized to create all experimental beams, including cooling, slowing, repumping, and imaging beams needed for the operation of the magneto-optical trap and associated diagnostics.

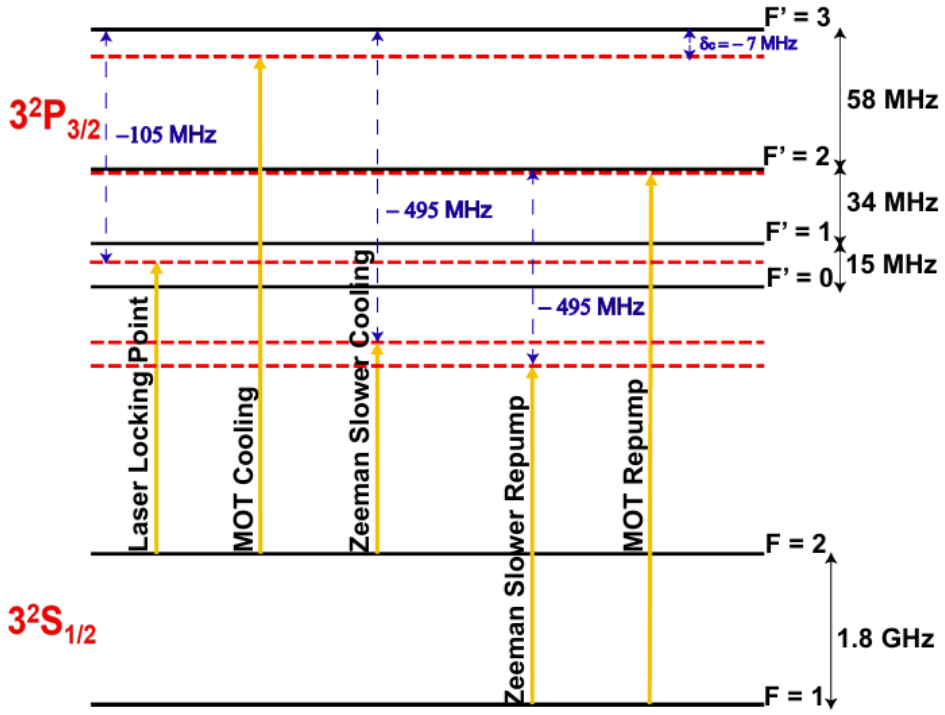

Figure 3.5: Energy level diagram of the sodium D_2 transition showing the laser frequency settings used for cooling, Zeeman slowing, and repumping in the experiment. The main laser system is frequency locked approximately 105 MHz below the $F' = 3$ excited-state level. The MOT cooling beam is detuned by $\delta_c = -7$ MHz from the cycling transition, while the Zeeman slower cooling beam is detuned by approximately -495 MHz to compensate for the large Doppler shifts of the fast atomic beam. Separate repumping beams are used to drive the $F = 1 \rightarrow F' = 2$ transition and return atoms to the cooling cycle. The hyperfine splittings of the excited and ground-state manifolds are also indicated.

The stable control of the laser frequency is critical for the efficient laser cooling. In this present experiment, the laser is locked to the red of the $F = 2 \rightarrow F' = 3$ cycling transition, at a detuning of 105 MHz. The laser frequency fluctuations or long-term drifts will have a large impact on the

rates of atom loading, cooling and MOT stability. There are several reasons for laser instability: mechanical stress, vibrations of the optical table, thermal drift, electronic offsets, and fluctuations in the optical system alignment. Thus, it is essential to have active frequency stabilization for reliable experimental operation.

The frequency is stabilized by FM modulation of the saturation absorption spectrum in a sodium vapor cell (Precision Glassblowing TG-ABNA, Pyrex, 25 mm OD $\times$ 75 mm path length). The vapor cell is heated to about 120 °C, to create enough density of sodium vapor for spectroscopy. A weak probe beam is sent through the vapor cell and a stronger counter-propagating pump beam produces Doppler-free saturation absorption features. In the spectroscopy setup, a double-passed 80 MHz acousto-optic modulator (AOM) is used to modulate the optical frequency with parameters $\nu_o = 160$ MHz, $\Delta\nu \approx 4$ MHz, and $\omega_{\text{ref}} = 2\pi \times 30$ kHz.

The modulation signal from the absorption of the probe beam is detected by a lock-in amplifier and an error signal proportional to the derivative of the Doppler-free Lamb dips is produced. The frequency-shifted laser is then stabilized by a home-built analog PID feedback circuit locked to the zero crossing point of the $F = 2 \rightarrow F' = 3$ crossover resonance. This causes the main cooling laser to be stabilized about 105 MHz below the $F' = 3$ excited-state transition.

The cooling laser beams are detuned by about $\delta_c = -7$ MHz from the red of the cycling transition during the loading of the MOT. MOTs have also been operated using the $F = 1 \rightarrow F' = 0$ transition, but these MOTs tend to have lower atomic densities [26, 27]. In Zeeman slowing, the detuning of the slowing beam is made much larger, about -495 MHz, to the red side of the $F = 2 \rightarrow F' = 3$ resonance to compensate for the large Doppler shift of the atomic beam that is ejected from the oven at high speed. All the frequency settings for the repumping beams used in the experiment are summarized in Fig. 3.3.

The second optical path from the TA-SHG Pro laser is used to create the Zeeman slowing beam described in Section 3.2.3, and the three orthogonal pairs of counter-propagating MOT beams for atom trapping in the experimental chamber. The MOT beams are circularly polarized and red-detuned from the cycling transition to allow for Doppler cooling [28]. The cooling beams are not the only ones used for imaging the atomic cloud: there are also separate imaging beams for absorption imaging and fluorescence imaging of the atomic cloud, which will be discussed in detail in Chapter 4.

There is also a corresponding repumping beam for each cooling related beam in the experiment. The repumping light is used to pump back atoms that fall to the hyperfine $F = 1$ ground state,

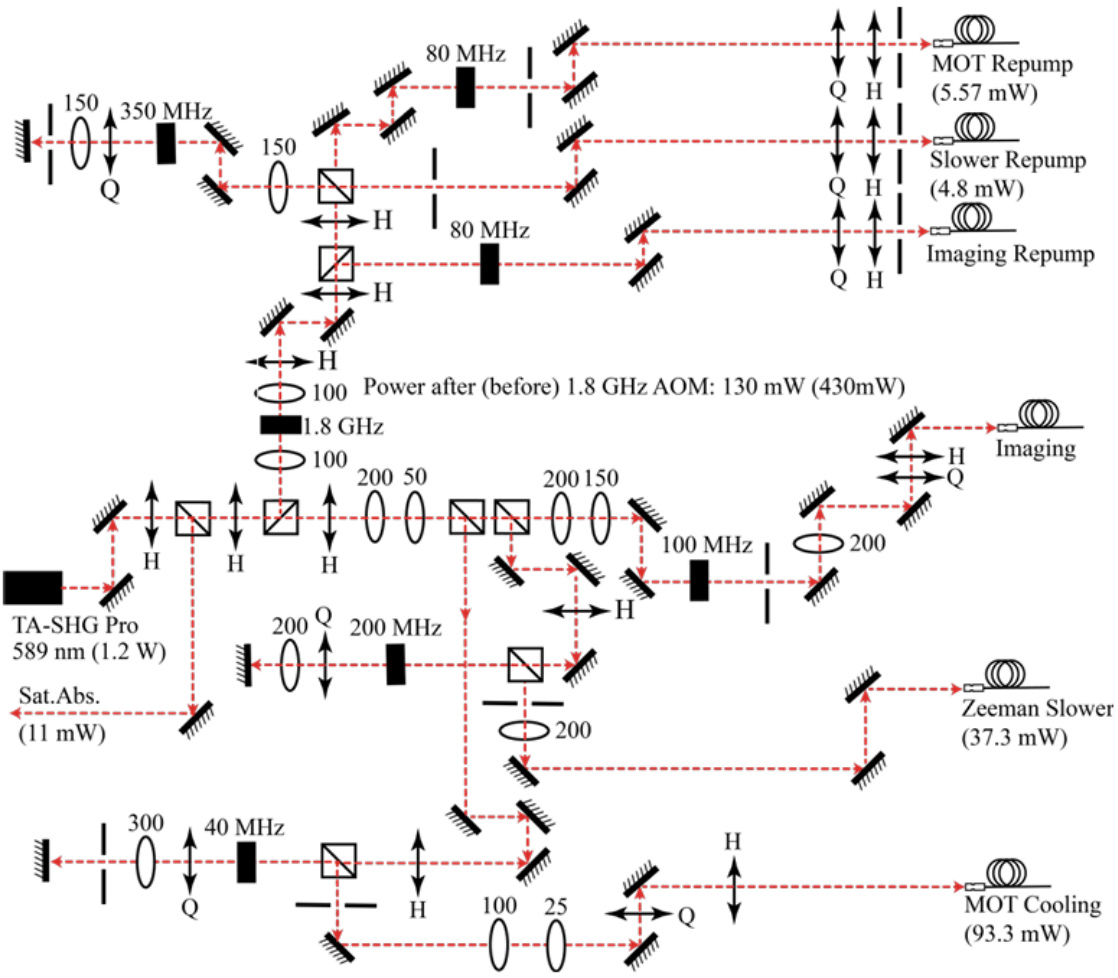

Figure 3.6: Schematic diagram of the laser distribution system used for generating the cooling, repumping, Zeeman slowing, and imaging beams in the experiment. The primary laser source is a frequency-doubled diode laser operating at 589 nm (TA-SHG Pro, 1.2 W). Acousto-optic modulators (AOMs), wave plates, beam splitters, lenses, and polarization optics are used to generate the required frequency detunings and independently control the optical power of each beam. Separate optical paths are used for the MOT cooling beam, Zeeman slower beam, imaging beam, and their corresponding repumping beams. Polarization-maintaining optical fibers transfer the beams from the laser table to the experiment table while preserving beam alignment stability.

and to drive the $F = 1 \rightarrow F' = 2$ transition. If light is not removed, atoms would build up in the $F = 1$ state and not be involved in the laser cooling transitions. All the cooling and repumping beams are generated by the optical arrangement shown in a schematic way in Fig. 3.4 and in an experimental way in Fig. 3.5. These optical systems employ acousto-optic modulators to independently control the frequencies and amplitudes of the beams, and mechanical shutters are used to completely extinguish individual beams as needed in the experimental timing sequences.

All laser beam generation optics are mounted on a special $5' \times 10'$ optical table. The produced beams are then transferred from the laser table to the experimental setup by polarization maintaining optical fibers. This setup makes optical alignment easier and provides the flexibility

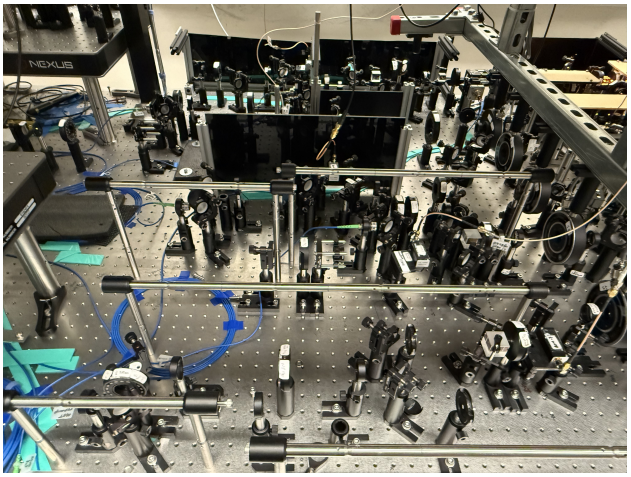

(a)

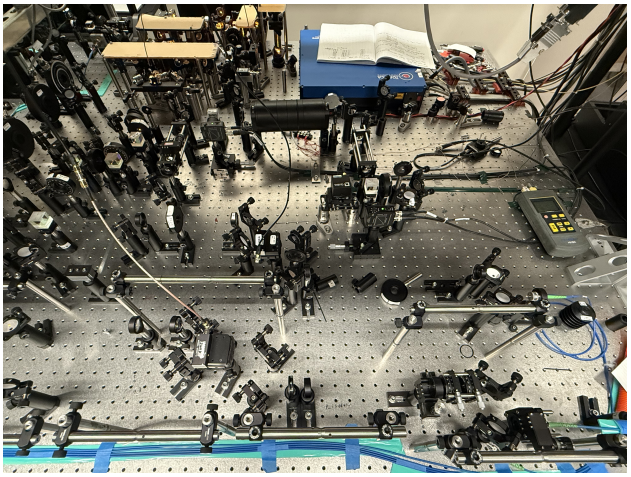

(b)

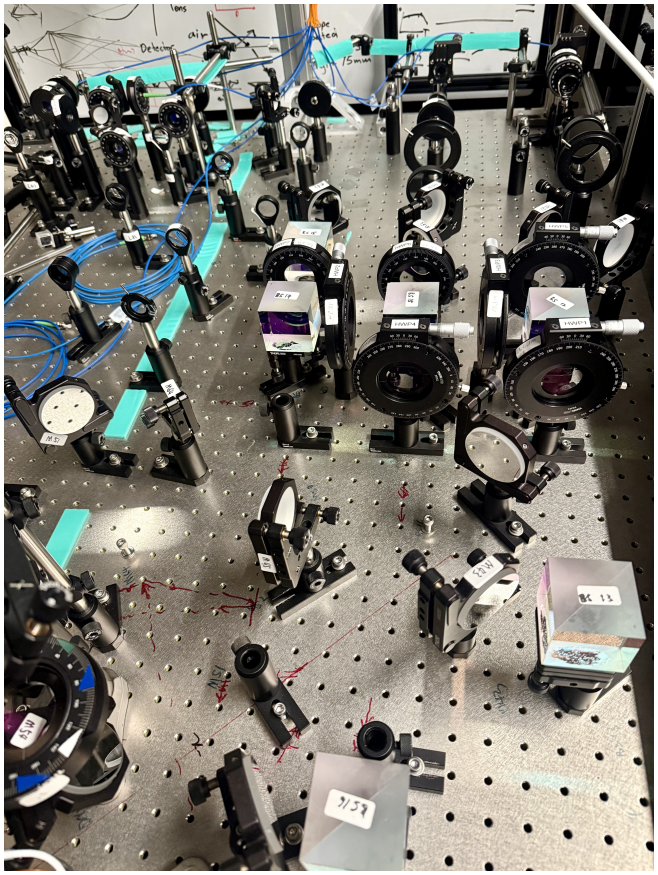

(c)

Figure 3.7: Optical layouts used for beam generation, delivery, and imaging in the ultracold sodium atom experiment. (a) and (b) Laser distribution optics on the optical table used for generating the cooling, repumping, slowing, and imaging beams required for MOT operation. (c) Imaging and beam delivery optics near the science chamber used for absorption imaging, beam alignment, and characterization of the ultracold atomic cloud.

to make changes or realign the laser system without interfering with the beam alignment at the experiment table.

The MOT repumping beams are split into two pairs of counter-propagating beams. The polarization and optical power of each of the six MOT beams are independently controlled with large 2" polarizing beam splitter and 1.5" $\lambda/2$ wave plates on the experiment table. The configuration of Fig. 3.7 is used to direct the beams into the vacuum chamber, with the large 2" mirrors. The diameter of each MOT beam is 1.25" to ensure a large trapping volume and efficient trapping of atoms. The experimental images of the optical table, atomic beam fluorescence and MOT fluorescence are displayed in Fig. 3.5.

3.3.2 AOMs and Mechanical Shutters

Laser intensity and frequency must be controlled precisely over the course of the experiment, especially during some of the more advanced cooling stages employed to reach sub-Doppler temperatures. Acousto-optic modulators (AOMs) as illustrated in Fig. 3.5 and Fig. 3.6 play a very important role in the present setup as they enable the rapid modulation of the optical power and frequency detuning of the experimental laser beams.

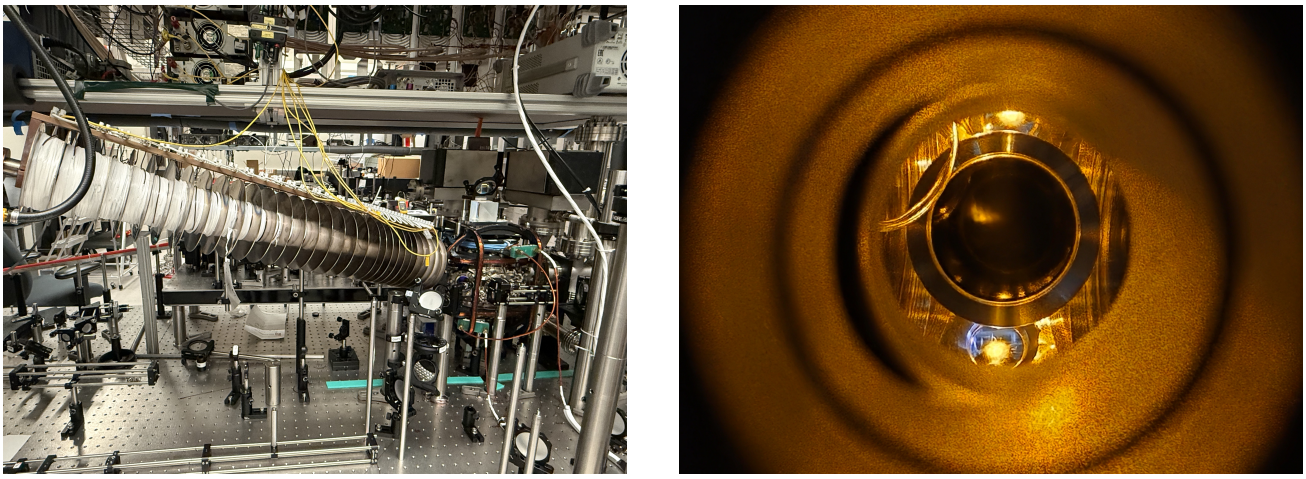

(a) (b)

Figure 3.8: Experimental vacuum apparatus and MOT beam used in the ultracold sodium atom experiment. (a) Photograph of the complete experimental setup including the Zeeman slower assembly, segmented cooling structure, MOT region, and main science chamber mounted on the optical table. (b) Fluorescence image of the Sodium MOT observed through the chamber viewport during operation of the MOT.

The switching times of the AOMs are in the nanosecond range, and they can be used as very fast optical switches in experimental timing sequences. The AOMs are able to attenuate the laser beams quickly, but there is still some leakage light even with the RF drive off. The mechanical shutters are used in conjunction with the AOMs to completely remove this residual light. The

switching time for the shutters is in the millisecond range and must be carefully synchronized to the overall timing sequence of the experiment.

Different AOMs from ISOMET and Gooch & Housego are used in the experiment, ranging from 40 MHz to 250 MHz, to produce the necessary optical detunings for cooling and trapping. The RF drivers used were from Isomet, Gooch & Housego and Intra-action. To produce repumping beams for which the frequency shift is larger and is near ~ 1.8 GHz, a high-frequency AOM (Brimrose GPF-1800-200-589) with a center frequency of 1.8 GHz and a bandwidth of 200 MHz is employed. This AOM is controlled with a custom RF driver system that includes an Agilent synthesizer and a Mini-Circuits 4 W RF amplifier.

In the following chapter, the imaging system developed for characterization of the ultracold sodium cloud will be discussed in detail.

Chapter 4

Imaging System Design

4.1 Introduction

Ultracold atomic gases, such as magneto-optical traps (MOTs) and Bose–Einstein condensates (BECs), are confined within ultra-high vacuum chambers and have dimensions ranging from a few micrometers to several millimeters [29]. Because these atomic samples are isolated from their surroundings and cannot be probed directly using conventional measurement tools, optical imaging techniques provide one of the most effective methods for interrogating the atomic cloud and extracting quantitative information about its properties. Parameters such as cloud size, shape, optical density, atom number, and spatial distribution can all be determined through carefully designed imaging systems [30].

In my experiment, imaging plays a critical role in the study of ultracold sodium atoms and their spin dynamics. To accurately characterize the atomic cloud and monitor its evolution, I designed, assembled, and characterized a dedicated imaging system capable of relaying high-quality images of the trapped atoms onto a scientific CCD camera. The imaging system was developed while accommodating the spatial constraints of the experimental apparatus and was optimized to achieve the magnification and spatial resolution required for future investigations of spin-dependent phenomena in ultracold sodium gases.

The performance of any imaging system directly influences the quality and accuracy of the measurements that can be obtained from the atomic sample. Consequently, it is essential to characterize key imaging parameters such as magnification, spatial resolution, and image fidelity before quantitative measurements can be performed [31]. To evaluate the performance of the system, I experimentally determined the magnification and resolution using a USAF 1951 resolution target and compared the measured results with theoretical expectations. These measurements provide important benchmarks for assessing the imaging capabilities of the system

and establishing its suitability for our next generation atom experiments.

In this chapter, I describe the design, construction, and characterization of the imaging system developed for the sodium experiment. I first present the optical design and experimental configuration, followed by the alignment procedures used during system assembly. I then discuss the methods used to determine the magnification and spatial resolution of the imaging system and compare the experimental results with theoretical predictions. Finally, I provide an overview of the imaging techniques employed to probe ultracold sodium atoms, which form the foundation for future studies of Bose–Einstein condensates and spin dynamics in this apparatus.

4.2 Theoretical Background

4.2.1 Optical Resolution

The ability of an imaging system to resolve fine spatial details is one of its most important performance characteristics. In ultracold atom experiments, the spatial resolution of the imaging system determines the smallest features that can be accurately observed in atomic density distributions and directly influences the precision of measurements such as cloud size, shape, and atom number. Consequently, understanding the theoretical limits of optical resolution is essential for evaluating the performance of the imaging system.

The fundamental limit of optical resolution is imposed by diffraction. When light passes through a finite aperture, the image of a point source is not formed as a perfect point on the detector. Instead, diffraction causes the light to spread into a characteristic intensity distribution known as an Airy pattern. The central bright region of this pattern, referred to as the Airy disk, defines the diffraction-limited resolution of the optical system (see Figure 4.1) [31].

The ultimate spatial resolution of an optical imaging system is fundamentally limited by diffraction. Even an ideal lens cannot focus light from a point source into an infinitely small point; instead, the image is formed as a diffraction pattern known as an Airy disk. The criterion most commonly used to define the minimum resolvable separation between two point sources is the Rayleigh criterion [32, 33]. According to this criterion, two point sources are considered just resolvable when the central maximum of one Airy pattern coincides with the first minimum of the other.

The resolving power of a lens is determined by its numerical aperture (NA), which characterizes the range of angles over which light can be collected. For a lens operating in air, the numerical aperture can be approximated as

$$NA = \frac{r}{f}, \tag{4.1}$$

where r is the radius of the lens aperture and f is the focal length. A larger numerical aperture corresponds to a greater light-gathering capability and improved spatial resolution.

Under the Rayleigh criterion, the radius of the Airy disk is given by

$$R = 1.22\frac{\lambda}{NA}, \tag{4.2}$$

where λ is the wavelength of the imaging light. The minimum resolvable distance is therefore directly proportional to the imaging wavelength and inversely proportional to the numerical aperture. Consequently, shorter wavelengths and larger numerical apertures produce smaller diffraction patterns and improve the resolving capability of the imaging system. This diffraction-limited resolution represents the theoretical upper limit of the imaging performance and serves as an important design consideration for absorption imaging of ultracold atomic clouds.

Although diffraction establishes the theoretical limit, the performance of a practical imaging system is often further constrained by optical aberrations, lens imperfections, alignment errors, and detector limitations. As a result, experimental characterization is necessary to determine the actual resolution achieved by the imaging system. In this work, I experimentally determined the spatial resolution using a USAF 1951 resolution target and compared the measured performance with theoretical expectations based on diffraction-limited imaging.

4.2.2 Absorption Imaging

Absorption imaging is the primary technique used in this experiment to obtain quantitative information about ultracold sodium atom clouds. The method has become a standard diagnostic tool in ultracold atom experiments because it provides direct measurements of optical density, column density, cloud shape, and total atom number [34]. In addition, absorption imaging has been widely employed in studies of Bose–Einstein condensates and spinor condensates due to its ability to accurately measure atomic density distributions [29, 30].

In absorption imaging, a weak probe beam tuned near an atomic resonance is directed through the atomic cloud. Atoms absorb and scatter photons from the probe beam, reducing the transmitted intensity. The resulting shadow of the cloud is then relayed through an imaging system and recorded by a CCD camera. By comparing the transmitted intensity to the incident intensity,

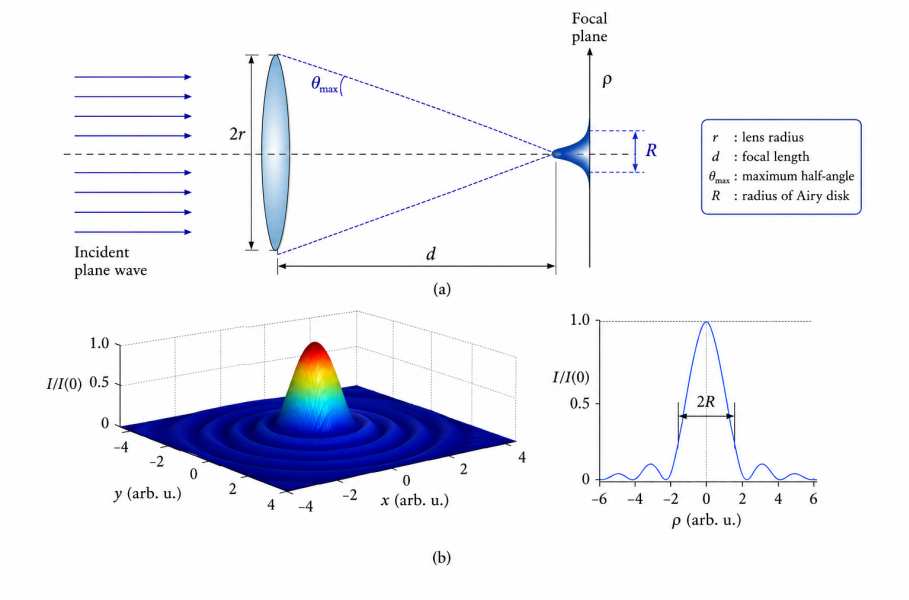

Figure 4.1: Physical parameters governing diffraction-limited imaging in a circular lens system. (a) Lens geometry illustrating the focal length (d), lens radius (r), and maximum convergence half-angle (max), which collectively determine the system numerical aperture. (b) Simulated Airy diffraction pattern generated by a circular aperture, shown as a three-dimensional intensity surface and radial cross-sectional profile. The Airy disk radius (R) corresponds to the first intensity minimum, while I/I denotes the normalized intensity distribution in the image plane.

the optical density distribution of the cloud can be calculated.

For probe intensities well below the saturation intensity, the transmission of light through the atomic cloud follows the Beer–Lambert law,

$$I(y,z) = I_0(y,z)\exp[-OD(y,z)], \tag{4.3}$$

where $I_0(y,z)$ is the incident intensity, $I(y,z)$ is the transmitted intensity, and $OD(y,z)$ is the optical density profile.

The optical density is related to the atomic column density through

$$OD(y,z) = \sigma \int_{-\infty}^{\infty} n(x,y,z)\,dx, \tag{4.4}$$

where $n(x,y,z)$ is the atomic number density, x is the propagation direction of the probe beam, and σ is the absorption cross section.

The absorption cross section depends on the properties of the imaging light and can be expressed as

$$\sigma = \frac{\sigma_0}{1 + 4\left(\frac{\Delta}{\Gamma}\right)^2 + \left(\frac{I}{I_{sat}}\right)}, \tag{4.5}$$

where σ_0 is the resonant absorption cross section, Δ is the detuning of the imaging beam from resonance, Γ is the natural linewidth of the atomic transition, I is the probe intensity, and I_{sat} is the saturation intensity [35]. In most absorption imaging experiments, the probe intensity is chosen to be significantly below the saturation intensity, allowing the saturation term to be neglected.

To determine the optical density experimentally, three images are acquired during each imaging sequence. The first image, I_{raw}, contains both the probe beam and the shadow of the atomic cloud. The second image, I_{ref}, is acquired using the same imaging pulse but without atoms present. A third image, I_{bg}, is obtained with the probe beam turned off and is used to remove detector offsets and stray background light. The optical density is then calculated as

$$OD(y, z) = \ln\left(\frac{I_{\text{ref}} - I_{\text{bg}}}{I_{\text{raw}} - I_{\text{bg}}}\right). \tag{4.6}$$

Once the optical density is known, the column density and total atom number can be calculated. Accurate determination of these quantities requires precise knowledge of the magnification and spatial resolution of the imaging system, motivating the characterization procedures presented later in this chapter.

A limitation of absorption imaging is that the resonant scattering process is destructive. The absorption and subsequent spontaneous emission of photons transfer momentum to the atoms, resulting in heating and modification of the atomic sample. Consequently, a new ultracold atom cloud or Bose–Einstein condensate must be prepared for each image acquisition when performing quantitative measurements [30].

4.3 Optical Design of the Imaging System

The imaging system was designed to provide optical access to the ultracold sodium atom cloud while accommodating the geometric constraints imposed by the vacuum chamber, magnetic coils, support structures, and surrounding optical components. Because the imaging path must coexist with multiple laser beams, viewports, and diagnostic instruments, careful planning of the optical layout was required before experimental implementation. To facilitate this process, I

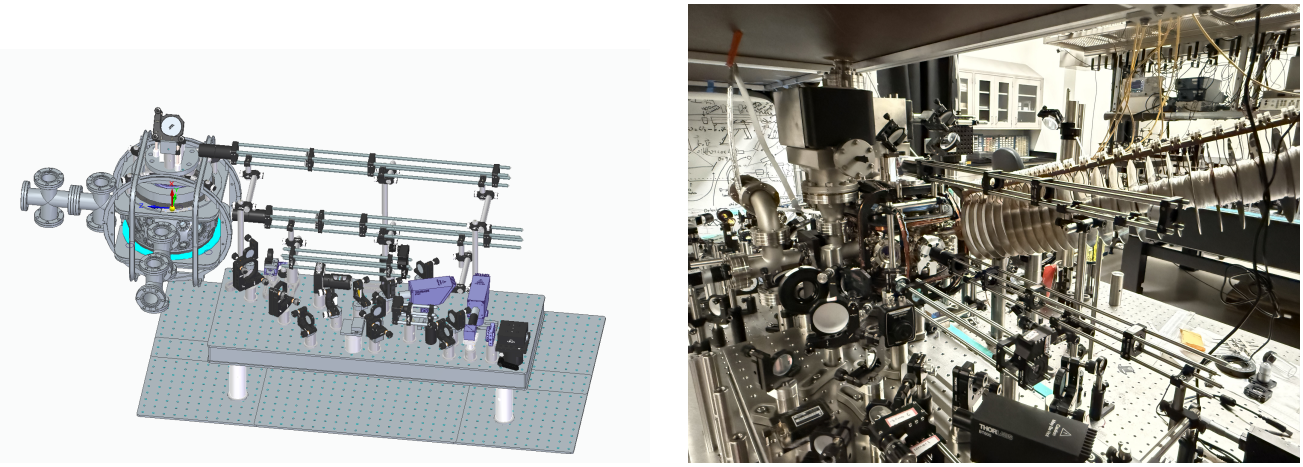

Figure 4.2: Comparison of the imaging system during the design and implementation stages. (a) Three-dimensional CAD model of the imaging system showing the vacuum chamber, optical rails, imaging optics, optomechanical mounts, and camera assembly used to optimize the optical layout and verify mechanical clearances prior to construction. (b) Photograph of the completed imaging system implemented in the laboratory, showing the assembled optical components mounted on rail systems around the ultrahigh-vacuum chamber for experimental characterization and future absorption imaging of ultracold sodium atoms.

first developed a complete three-dimensional computer-aided design (CAD) model of the imaging system and surrounding experimental apparatus, as shown in Fig. 4.2.

The CAD model was used to determine the physical placement of optical components, evaluate mechanical clearances, and verify that the imaging path could be integrated into the existing sodium apparatus without obstructing other experimental subsystems. The model included the vacuum chamber, optical rails, lens mounts, translation stages, mirrors, beam steering optics, and camera assembly. This virtual design environment enabled iterative optimization of component locations before physical construction, significantly reducing alignment challenges during system assembly.

The imaging system was designed as a relay telescope configuration positioned along one of the imaging ports of the vacuum chamber. The optical axis was aligned with the center of the trapping region to maximize light collection from the atomic cloud. Particular attention was given to maintaining adequate working distances between the chamber viewport and the first imaging lens while preserving sufficient space for mechanical adjustments and future system modifications.

The lens configuration was selected to provide a magnification of approximately $0.6\times$, which is suitable for imaging the relatively large spatial extent of the magneto-optical trap. This magnification allows the entire atomic cloud to be projected onto the CCD sensor without cropping while simultaneously providing adequate spatial sampling for quantitative measurements.

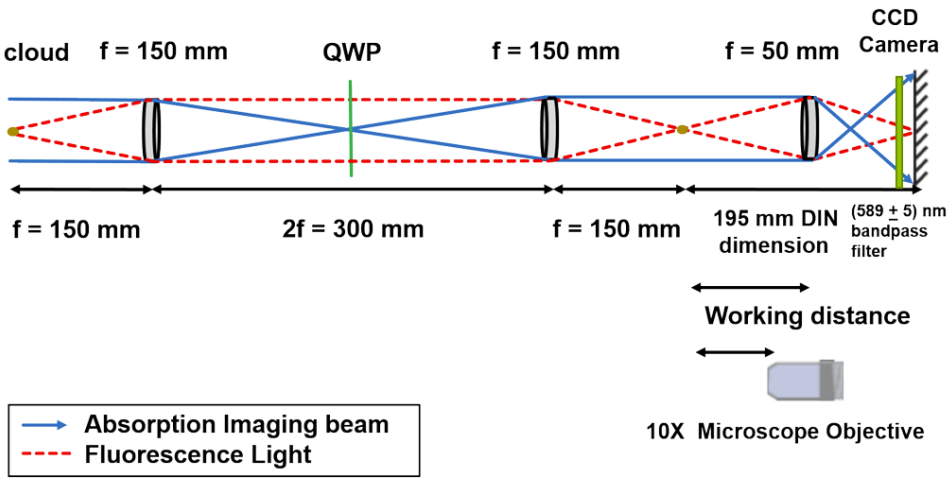

Figure 4.3: Three-dimensional representation of the optical imaging configuration employed for imaging ultracold sodium atomic clouds. The imaging train comprises achromatic relay lenses, a quarter-wave plate (QWP), a 10× microscope objective, a (589 ± 5) nm bandpass filter, and a CCD camera. Blue solid rays denote the absorption imaging beam, while red dashed rays illustrate fluorescence collection. The optical arrangement forms successive image planes to achieve the required magnification and spatial resolution for diffraction-limited imaging of the atomic cloud.

The relay imaging geometry was also designed to minimize optical aberrations and maintain image quality across the field of view.

Following completion of the CAD design, the imaging system was assembled on the optical table using the specified optomechanical components and aligned with the vacuum chamber. The CAD model served as a blueprint during construction, allowing component positions to be transferred directly from the virtual design to the experimental setup. Fine alignment was subsequently performed using alignment targets and test objects to ensure that the optical axis intersected the center of the trapping region and that the image plane coincided with the CCD sensor.

The completed imaging system provides a stable and reproducible platform for quantitative absorption imaging of ultracold sodium atoms. Furthermore, the modular design allows future modifications, including the incorporation of higher-magnification optics for Bose–Einstein condensate imaging and spin-sensitive measurements. The magnification and spatial resolution of the assembled system were subsequently characterized experimentally using a USAF 1951 resolution target, as described in the following sections.

4.4 Implementation of the Imaging System

Following completion of the optical design and CAD modeling, the imaging system was assembled on the optical table and integrated with the sodium vacuum chamber. The final experimental configuration closely followed the CAD design shown in Fig. 4.2, which served as the primary reference during construction. The CAD model allowed the locations of optical components, support structures, and mounting hardware to be determined prior to assembly, reducing the need for extensive modifications during implementation.

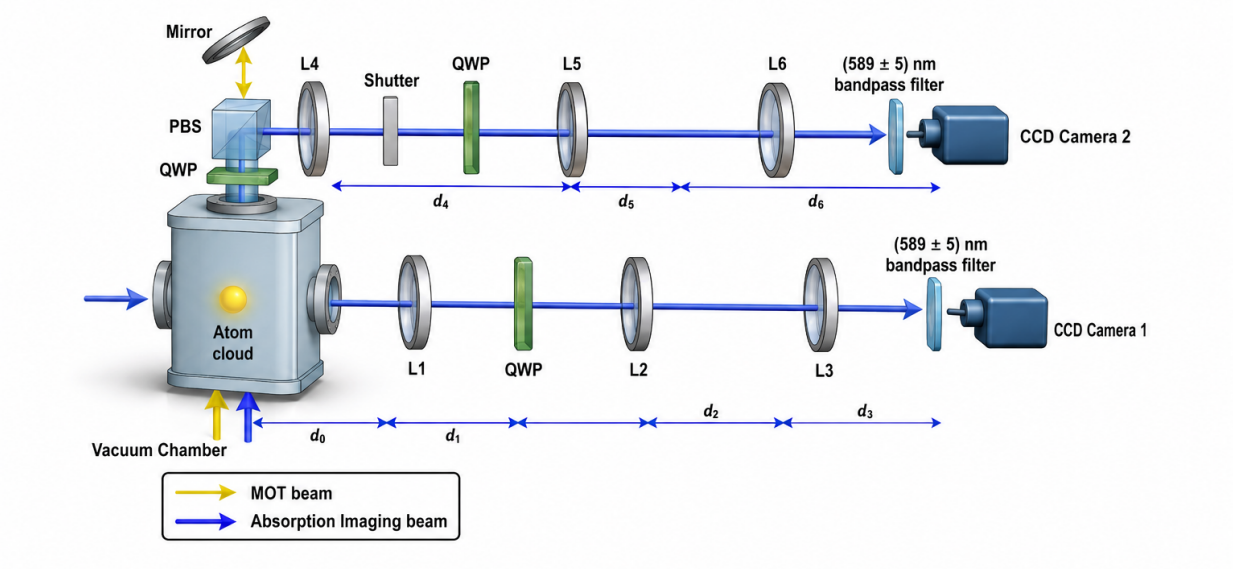

Figure 4.4: Three-dimensional optical layout of the dual-view imaging system used for absorption imaging of ultracold sodium atoms. The system consists of independent side- and top-imaging pathways employing relay lenses, quarter-wave plates (QWPs), a polarization beam splitter (PBS), a steering mirror, narrowband 589 nm bandpass filters, and CCD cameras. The optical arrangement enables simultaneous imaging along orthogonal directions while preserving the required magnification and spatial resolution. Yellow arrows indicate magneto-optical trap (MOT) beams and blue arrows denote the absorption imaging beam.

The imaging system was installed along a side viewport of the vacuum chamber to provide direct optical access to the trapped sodium atom cloud. The optical axis was aligned with the center of the trapping region using alignment targets and low-power laser beams. Particular care was taken to ensure that the imaging axis intersected the center of the atom cloud while maintaining sufficient clearance from the surrounding magnetic coils, vacuum hardware, and laser beam paths.

The imaging optics were mounted on a rigid rail-based support structure to provide mechanical stability and maintain alignment over extended periods of operation. Lens mounts, translation stages, and optical posts were positioned according to the dimensions specified in the CAD design. During assembly, each optical component was installed sequentially and aligned relative to the

vacuum chamber center to minimize optical aberrations and maximize image quality.

Table 4.1: Technical specifications of the PCO Pixelfly CCD camera used for image acquisition.

Parameter	**Value**
Detector type	CCD sensor
Quantum efficiency	62%
Wavelength sensitivity	290–1100 nm
Analog-to-digital resolution	14-bit
Pixel pitch	6.45 μm $\times$ 6.45 μm
Sensor resolution	1392 $\times$ 1040 pixels
Dark current	1 e^-/pixel/s at 23°C
Charge capacity	1.6×10^4 e^-
Camera dimensions	39 mm $\times$ 39 mm $\times$ 71 mm
Dual-image acquisition mode	Two consecutive frames with $\sim$ μs separation

To evaluate the performance of the imaging system prior to atom imaging experiments, a USAF 1951 resolution target was positioned at the location corresponding to the atomic cloud. A collimated 589 nm TA-SHG Pro laser beam was used as the illumination source during these measurements. The resulting images were recorded using a PCO Pixelfly CCD camera with a pixel size of 6.45 µm $\times$ 6.45 µm. The camera was mounted on a precision translation stage that allowed fine adjustment along the optical axis for accurate focusing. Additional transverse adjustments were used to center the image on the detector and optimize image quality.

The alignment procedure was performed iteratively by monitoring the image sharpness of the resolution target while adjusting the positions of the imaging optics and camera [36]. Fine alignment of the optical axis was achieved by maximizing image contrast and minimizing distortion across the field of view. Once optimal alignment was obtained, all optomechanical components were securely fixed in place to ensure long-term stability and reproducibility of measurements.

The completed imaging system provided a robust platform for quantitative characterization of magnification and spatial resolution. The experimentally assembled configuration closely matched the design specifications predicted during the CAD modeling stage, demonstrating the effectiveness of the design process. The performance of the system was subsequently evaluated through magnification and resolution measurements, which are presented in the following chapter.

Chapter 5

Imaging System Characterization

5.1 Introduction

After completing the design and implementation of the imaging system described in Chapter 4, I experimentally characterized its performance to determine the key imaging parameters required for ultracold atom experiments. Although the optical design provided estimates of the expected magnification and resolution, it was necessary to verify these values experimentally using acquired images. This characterization also allowed me to evaluate the overall image quality and assess how well the system could resolve fine spatial features.

To perform these measurements, I imaged a USAF 1951 resolution target using the completed imaging system and analyzed the resulting images. The acquired data were used to determine the system magnification, evaluate its spatial resolution, and examine the contrast of progressively smaller features through intensity profile analysis. Multiple measurements were performed to assess the repeatability of the results and estimate the associated uncertainties. The procedures and results presented in this chapter establish the experimental performance of the imaging system and provide the calibration parameters required for future absorption imaging of ultracold sodium atoms.

5.2 Experimental Image Acquisition

Following the assembly, alignment, and calibration of the imaging systems, I acquired a series of images to evaluate the performance of each imaging configuration. Four imaging configurations were tested: a side imaging system with a magnification of $M = 0.6$, a top imaging system with a magnification of $M = 0.6$, a top imaging system with a magnification of $M = 4$, and a side imaging system with a magnification of $M = 10$. The two imaging systems with $M = 0.6$ were designed for imaging the magneto-optical trap (MOT), where a larger field of view is needed to

capture the entire atom cloud. The imaging systems with $M = 4$ and $M = 10$ were designed for imaging the Bose–Einstein condensate (BEC), where higher magnification is required because of the much smaller size of the condensate.

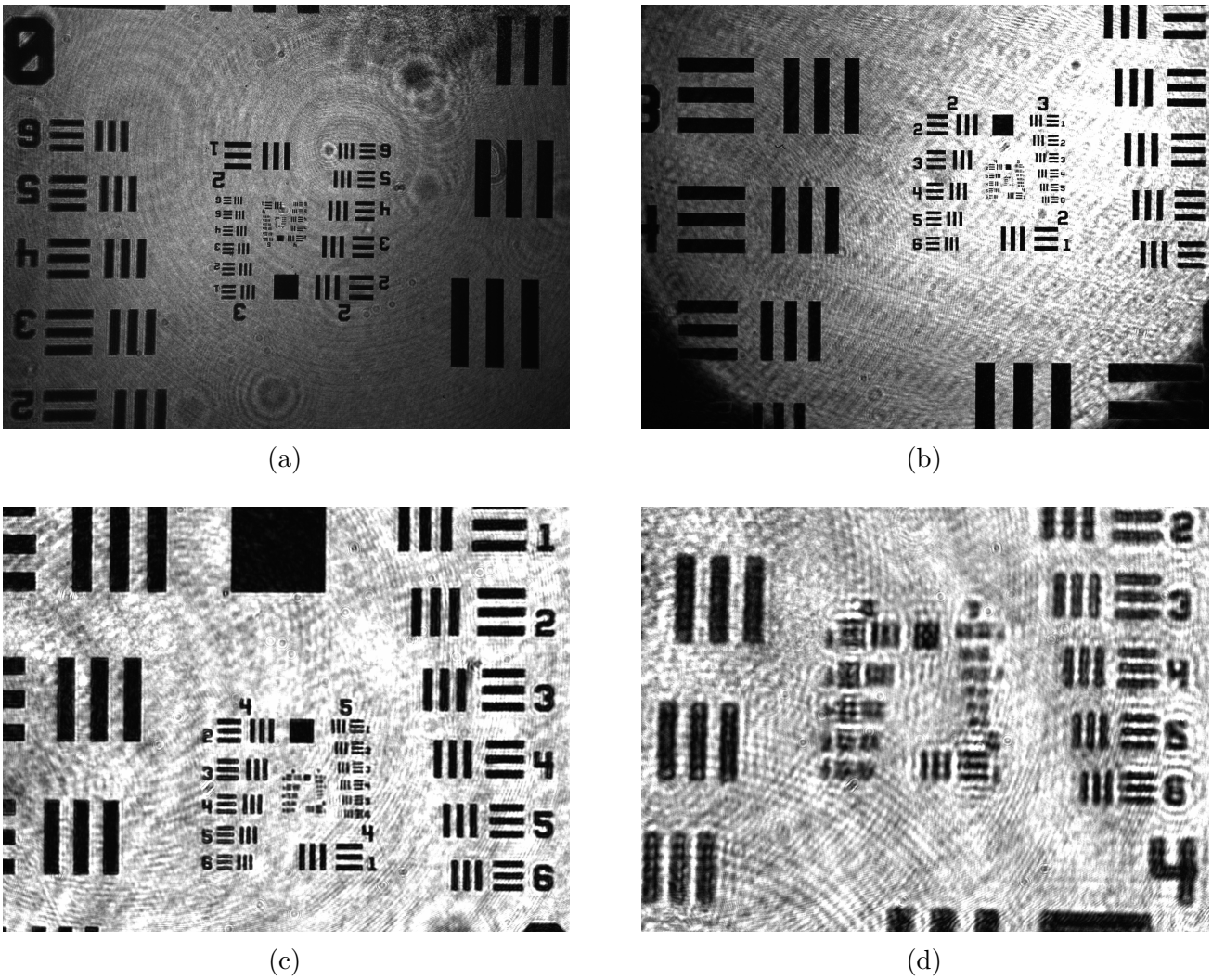

(a) (b)

(c) (d)

Figure 5.1: Representative images of the USAF 1951 resolution target acquired using the four imaging configurations investigated in this work: (a) side imaging system at $M = 0.6$, (b) top imaging system at $M = 0.6$, (c) top imaging system at $M = 4$, and (d) side imaging system at $M = 10$. These images were used for magnification calibration, spatial resolution measurements, and intensity profile analysis.

To characterize the imaging performance, I used a USAF 1951 positive resolution target as the calibration object. This target contains groups and elements with known spatial frequencies, making it suitable for measuring both the magnification and the spatial resolution of the imaging systems. Before acquiring images, I carefully positioned the target at the object plane of each imaging system and adjusted the alignment until the target was centered in the field of view and brought into sharp focus.

The target was illuminated using an expanded laser beam to provide nearly uniform illumination over the entire imaging area. The transmitted light was collected by the imaging optics and

recorded using a pco.pixelfly CCD camera with a sensor resolution of 1392×1040 pixels and a pixel size of 6.45 μm. For each imaging configuration, I adjusted the camera exposure time and gain to obtain good image contrast while avoiding saturation of the CCD sensor. During the alignment process, I recorded multiple images and selected the sharpest images with the best overall contrast for the quantitative analysis presented in the following sections.

Figure 5.1 shows representative images of the USAF 1951 resolution target acquired using the four imaging configurations. The target contains features with different spatial frequencies, making it useful for comparing the performance of the imaging systems. In all four configurations, the larger line-pair elements are clearly visible, while the finer features become increasingly difficult to resolve as the spatial frequency increases. The higher-magnification imaging systems ($M = 4$ and $M = 10$) produce a much larger image of the target than the two systems with $M = 0.6$, making the finer line pairs easier to observe and analyze.

I used these images for all of the quantitative analyses presented in the following sections. First, I measured the pixel distances between selected target features to determine the magnification of each imaging configuration. Next, I identified the smallest line-pair element that could still be clearly resolved to estimate the experimental spatial resolution. Finally, I extracted intensity profiles across selected line pairs to examine how the image contrast changed as the spatial frequency increased. These measurements allowed me to evaluate the performance of each imaging configuration and verify that they are suitable for future absorption imaging of ultracold sodium atoms.

5.3 Analysis of the Obtained Images

5.3.1 Magnification Measurement

The magnification of each imaging configuration was determined using the USAF 1951 resolution target. Pixel distances corresponding to two line pairs were measured at multiple locations on the target image and converted to physical distances using the CCD pixel size of 6.45 μm. The magnification was then calculated as the ratio of the measured image size to the known object size. For each imaging configuration, the mean magnification was calculated from repeated measurements, and the uncertainty was first estimated using the 95% confidence interval of the mean.

To account for additional sources of uncertainty associated with the camera pixel size and the calibrated dimensions of the USAF resolution target, the magnification uncertainty was also

estimated using first-order Gaussian error propagation [37, 38]. The propagated uncertainty was calculated as

$$\sigma_M = \sqrt{\left(\frac{\partial M}{\partial p}\sigma_p\right)^2 + \left(\frac{\partial M}{\partial s}\sigma_s\right)^2 + \left(\frac{\partial M}{\partial d}\sigma_d\right)^2}, \tag{5.1}$$

where p is the measured pixel distance, s is the camera pixel size, and d is the spacing of two line pairs on the USAF 1951 resolution target. The measured magnifications for the four imaging configurations are summarized in Table 5.1.

Table 5.1: Measured magnifications of the four imaging configurations. The first uncertainty represents the 95% confidence interval obtained from repeated measurements, while the second uncertainty was calculated using first-order Gaussian error propagation.

Imaging configuration	**95% Confidence Interval**	**Gaussian Error Propagation**
Side imaging ($M = 0.6$)	0.653 ± 0.026	0.653 ± 0.033
Top imaging ($M = 0.6$)	0.521 ± 0.012	0.521 ± 0.016
Top imaging ($M = 4$)	4.094 ± 0.026	4.094 ± 0.060
Side imaging ($M = 10$)	10.82 ± 0.09	10.82 ± 0.17

The experimentally measured magnifications are in good agreement with the design values for all four imaging configurations. The side imaging system achieved a magnification of approximately $M = 0.65$, while the top imaging system operating in the low-magnification configuration produced a magnification of approximately $M = 0.52$. The two high-magnification imaging systems yielded magnifications of $M = 4.09$ and $M = 10.82$, respectively, both of which closely match their intended design magnifications of $M = 4$ and $M = 10$.

For all four imaging configurations, the uncertainties obtained using Gaussian error propagation are slightly larger than those estimated from repeated measurements alone because they include additional contributions from the uncertainty in the camera pixel size and the dimensions of the calibration target. Nevertheless, the two uncertainty estimation methods produced consistent results for every imaging configuration, demonstrating good repeatability of the measurements and confirming the accuracy of the magnification calibration.

The experimentally determined magnifications establish the relationship between distances measured on the CCD image and their corresponding dimensions in the object plane. These calibration factors will be used in future experiments to perform quantitative measurements of the size and spatial distribution of magneto-optical traps and Bose–Einstein condensates.

5.3.2 Intensity Profile Analysis

To further evaluate the resolving capability of the imaging systems, I extracted intensity profiles from selected elements of the USAF 1951 resolution target for the side imaging system operating at $M = 0.6$, the top imaging system operating at $M = 0.6$, the top imaging system operating at $M = 4$, and the side imaging system operating at $M = 10$. For each target element, I drew a line perpendicular to the line pairs and recorded the grayscale intensity values along the line as a function of distance. These intensity profiles provide a quantitative measure of how well each imaging configuration can distinguish adjacent bright and dark features as the spatial frequency increases.

For each imaging configuration, I adjusted the camera exposure time and gain independently to obtain good image contrast while avoiding saturation of the CCD camera. As a result, the absolute intensity values differ among the four datasets and should not be compared directly. Instead, I used the shape of the intensity profiles, particularly the separation between adjacent peaks and valleys, to evaluate the resolving performance of each imaging system.

Figures 5.2–5.5 show the intensity profiles obtained from the four imaging configurations. For the lower spatial-frequency elements, all four systems produce well-defined peaks and valleys, indicating that the bright and dark bars of the USAF target are clearly resolved. As the spatial frequency increases, the distance between adjacent peaks decreases and the modulation depth gradually becomes smaller, reflecting the finite resolving capability of each imaging system.

The side imaging system operating at $M = 0.6$ (Figure 5.2) clearly resolves the lower spatial-frequency elements, with distinct intensity oscillations observed up to approximately Group 5, Element 2. Beyond this point, the peaks become progressively less distinct, indicating that the system is approaching its practical resolution limit.

The top imaging system operating at $M = 0.6$ (Figure 5.3) exhibits similar behavior but maintains stronger peak-to-valley contrast at higher spatial frequencies. Clear intensity oscillations remain visible up to approximately Group 5, Element 5, demonstrating improved resolving capability compared with the side imaging system operating at the same magnification.

The top imaging system operating at $M = 4$ (Figure 5.4) provides further improvement by producing a larger image of the target. The increased magnification allows finer spatial features to be sampled by more camera pixels, resulting in better-defined intensity oscillations at high spatial frequencies. Distinct peaks remain visible up to approximately Group 5, Element 5 before the modulation begins to decrease for the highest-frequency elements.

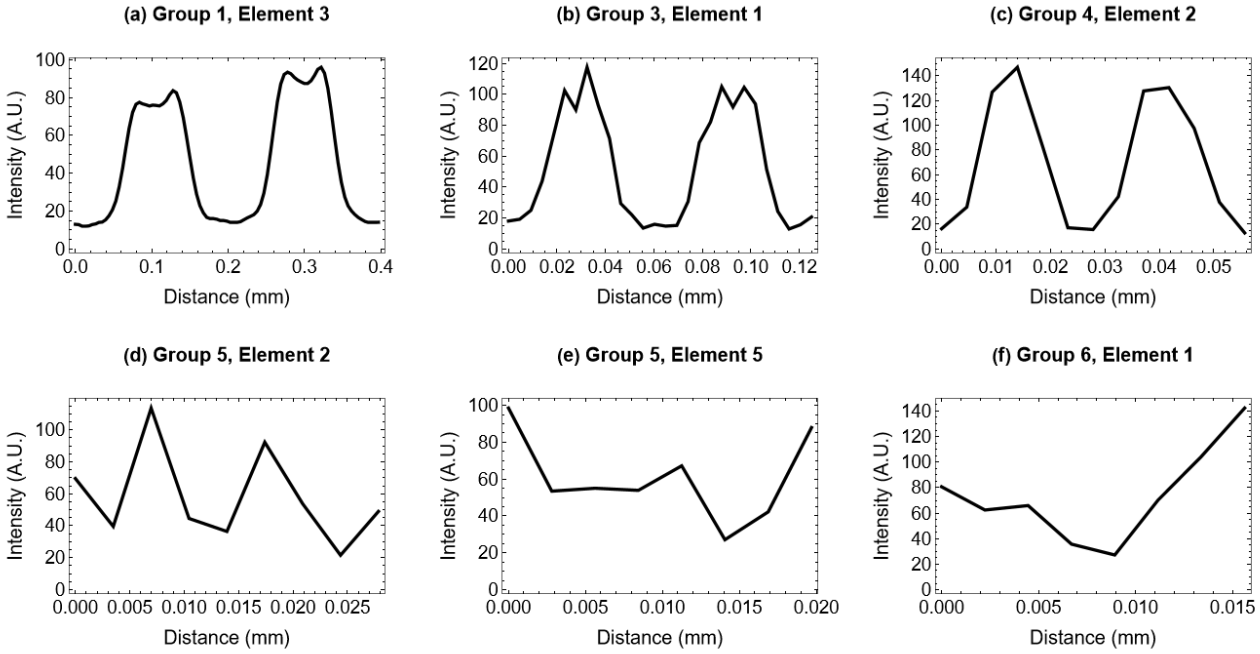

Figure 5.2: Intensity profiles extracted from selected elements of the USAF 1951 resolution target using the side imaging system at $M = 0.6$. The target elements are arranged in order of increasing spatial frequency from Group 1, Element 3 to Group 6, Element 1.

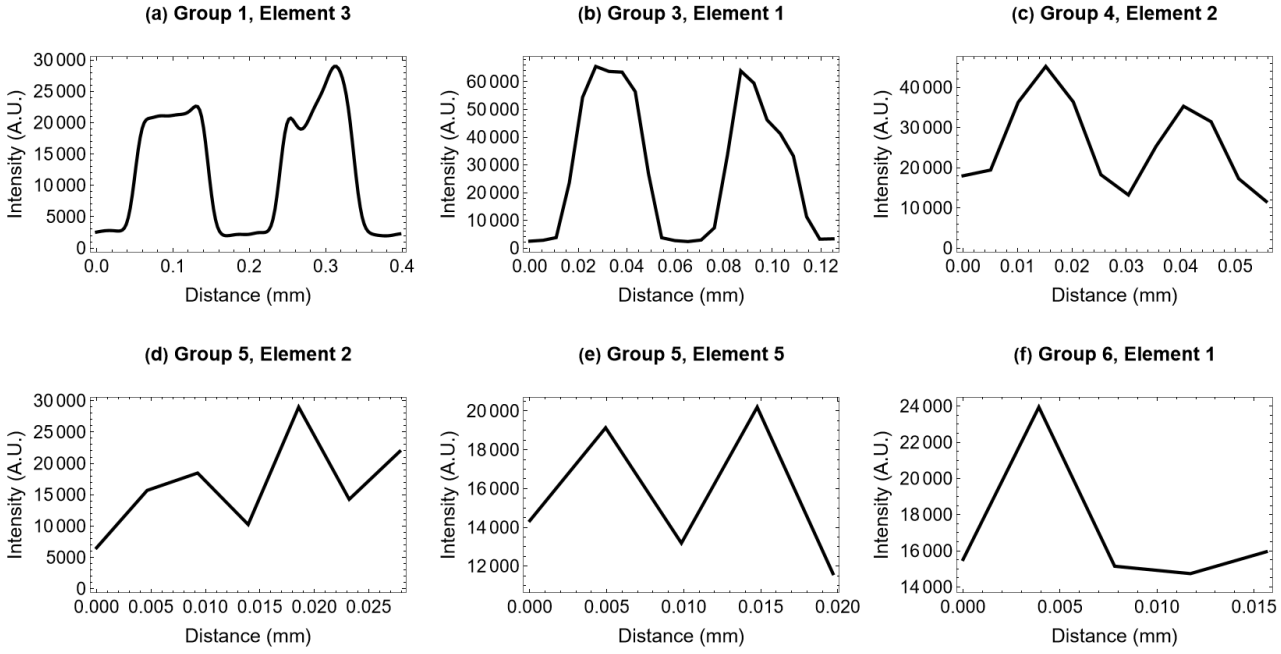

Figure 5.3: Intensity profiles extracted from selected elements of the USAF 1951 resolution target using the top imaging system at $M = 0.6$. The target elements are arranged in order of increasing spatial frequency from Group 2, Element 2 to Group 6, Element 1.

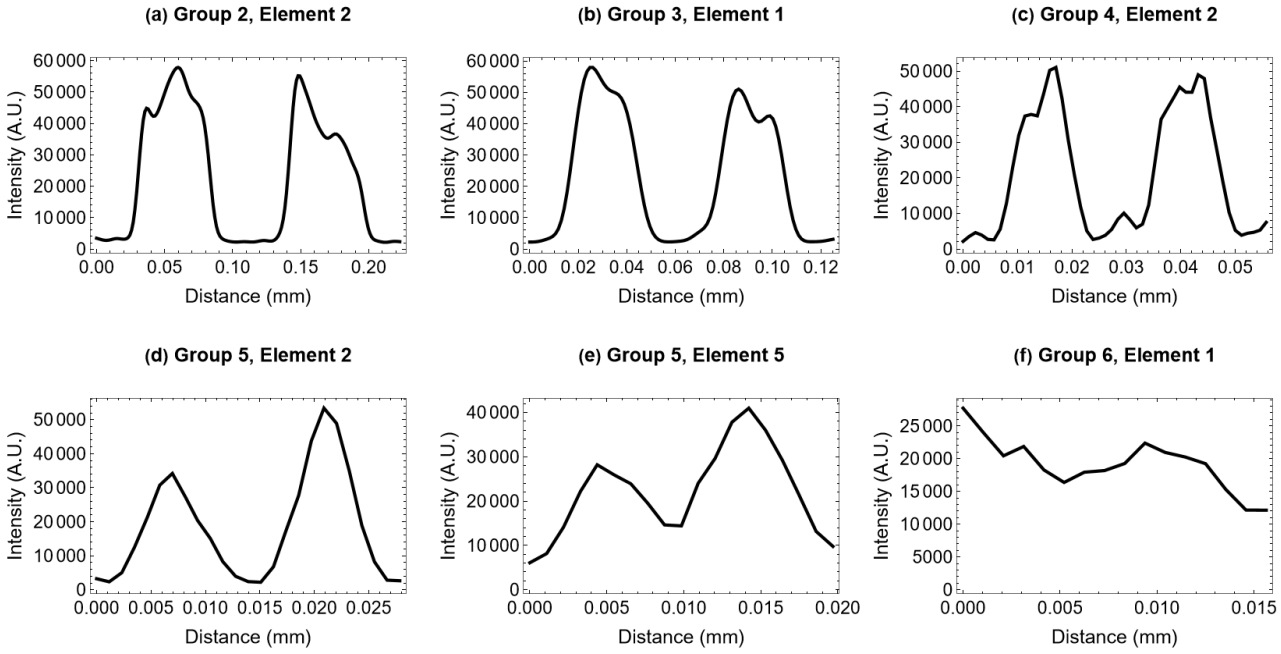

Figure 5.4: Intensity profiles extracted from selected elements of the USAF 1951 resolution target using the top imaging system at $M = 4$. The target elements are arranged in order of increasing spatial frequency from Group 1, Element 3 to Group 6, Element 1.

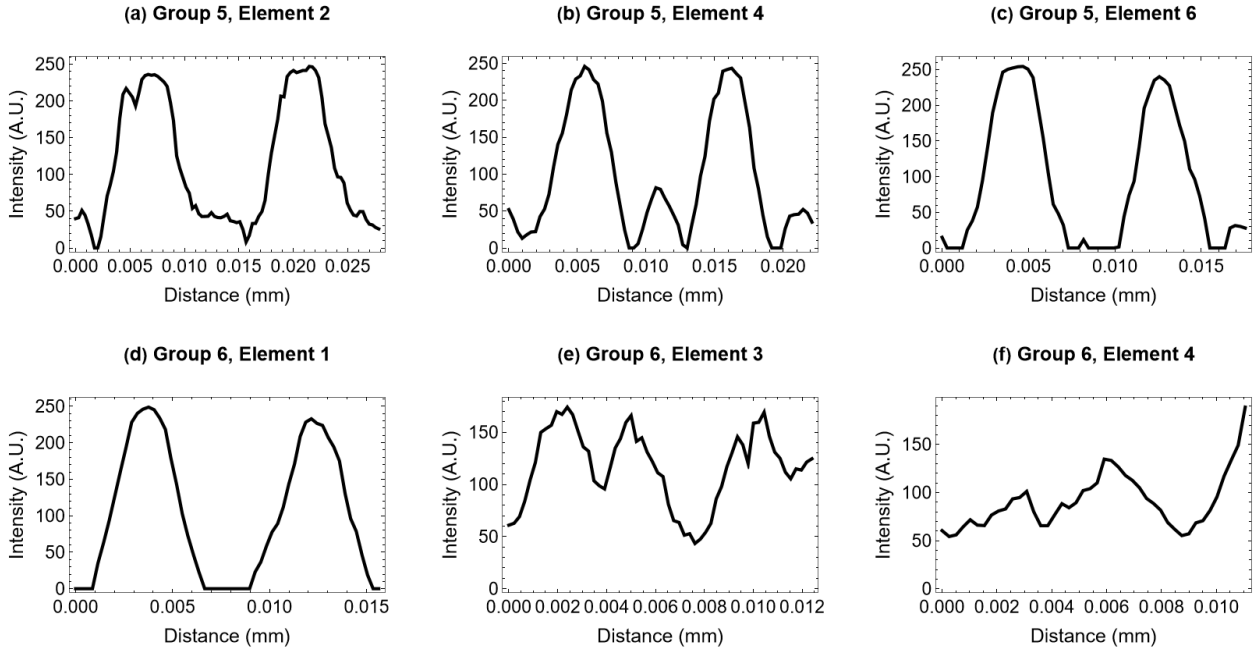

Figure 5.5: Intensity profiles extracted from selected elements of the USAF 1951 resolution target using the side imaging system at $M = 10$. The target elements are arranged in order of increasing spatial frequency from Group 5, Element 2 to Group 6, Element 4.

The highest resolving capability was obtained with the side imaging system operating at $M = 10$ (Figure 5.5). Even for Group 6 target elements, well-defined intensity peaks remain visible for several elements before gradually merging at the highest spatial frequencies. The increased image magnification allows the fine features of the USAF target to be sampled more effectively by the CCD camera, making this configuration the most suitable for resolving the smallest structures.

Overall, the intensity profile analysis provides a clear experimental comparison of the four imaging configurations. The gradual reduction in intensity modulation with increasing spatial frequency is consistent with the expected behavior of an optical imaging system approaching its resolution limit. The results also demonstrate the benefit of higher image magnification, with the $M = 10$ side imaging system providing the best resolving performance, followed by the $M = 4$ top imaging system, while the two $M = 0.6$ configurations provide sufficient resolution for imaging larger atomic clouds such as the magneto-optical trap.

5.3.3 Resolution Assessment with Rayleigh Criterion

To evaluate the resolving capability of the imaging systems, I determined both the theoretical and experimental spatial resolutions for each imaging configuration. The theoretical resolution was estimated using the Rayleigh criterion, while the experimental resolution was obtained from images of the USAF 1951 resolution target together with the corresponding intensity profile analysis presented in the previous section.

According to the Rayleigh criterion, two point sources are considered just resolved when the central maximum of one Airy diffraction pattern coincides with the first minimum of the adjacent diffraction pattern. The diffraction-limited resolution is given by

$$d = \frac{1.22\lambda}{NA}, \tag{5.2}$$

where λ is the imaging wavelength and NA is the numerical aperture of the imaging system.

For the side imaging system operating at $M = 0.6$, the top imaging system operating at $M = 0.6$, and the top imaging system operating at $M = 4$, the numerical aperture was approximately $NA = 0.10$. Using the sodium D_2 transition wavelength of $\lambda = 589$ nm, the theoretical diffraction-limited resolution is

$$d = \frac{1.22(589 \times 10^{-9})}{0.10} = 7.19 \times 10^{-6}\,\text{m} = 7.19\ \mu\text{m}. \tag{5.3}$$

The side imaging system operating at $M = 10$ employed a microscope objective with a numerical aperture of $NA = 0.25$. Therefore, the theoretical diffraction-limited resolution is

$$d = \frac{1.22(589 \times 10^{-9})}{0.25} = 2.87 \times 10^{-6}\,\text{m} = 2.87\ \mu\text{m}. \tag{5.4}$$

The experimental resolution was determined using the USAF 1951 resolution target by identifying the highest target element that remained clearly resolved in the intensity profile analysis. The side imaging system operating at $M = 0.6$ resolved features up to Group 5, Element 2, while both top imaging systems resolved features up to Group 5, Element 5. The side imaging system operating at $M = 10$ resolved features up to Group 6, Element 3.

The spatial frequency of a USAF 1951 target is given by

$$f_{\text{USAF}} = 2^{G+\frac{E-1}{6}}, \tag{5.5}$$

where G and E denote the group and element numbers.

For the side imaging system operating at $M = 0.6$,

$$f_{\text{USAF}} = 2^{5+\frac{2-1}{6}} = 35.92\ \text{lp/mm}, \tag{5.6}$$

which corresponds to a line-pair spacing of

$$d_{\text{lp}} = \frac{1}{35.92} = 27.84\ \mu\text{m}, \tag{5.7}$$

giving an experimentally resolved feature size of

$$d_{\text{exp}} = \frac{27.84}{2} = 13.92\ \mu\text{m}. \tag{5.8}$$

For the two top imaging systems,

$$f_{\text{USAF}} = 2^{5+\frac{5-1}{6}} = 50.80\ \text{lp/mm}, \tag{5.9}$$

which gives

$$d_{\text{lp}} = \frac{1}{50.80} = 19.69\ \mu\text{m}, \tag{5.10}$$

and therefore

$$d_{\text{exp}} = \frac{19.69}{2} = 9.84\ \mu\text{m}. \tag{5.11}$$

For the side imaging system operating at $M = 10$,

$$f_{\text{USAF}} = 2^{6+\frac{3-1}{6}} = 80.63\ \text{lp/mm}, \tag{5.12}$$

which corresponds to

$$d_{\text{lp}} = \frac{1}{80.63} = 12.40\ \mu\text{m}, \tag{5.13}$$

and therefore

$$d_{\text{exp}} = \frac{12.40}{2} = 6.20\ \mu\text{m}. \tag{5.14}$$

The theoretical and experimentally determined spatial resolutions are summarized in Table 5.2.

Table 5.2: Comparison of theoretical and experimentally measured spatial resolutions for the four imaging configurations.

Configuration	**NA**	**Theory (μm)**	**Highest USAF**	**Experiment (μm)**
Side ($M = 0.6$)	0.10	7.19	G5E2	13.92 ± 0.83
Top ($M = 0.6$)	0.10	7.19	G5E5	9.84 ± 0.60
Top ($M = 4$)	0.10	7.19	G5E5	9.84 ± 0.60
Side ($M = 10$)	0.25	2.87	G6E3	6.20 ± 0.38

Table 5.2 shows that the experimentally measured resolutions are larger than the corresponding theoretical Rayleigh limits for all four imaging configurations. This difference is expected because the Rayleigh criterion describes the performance of an ideal diffraction-limited optical system, whereas the experimentally measured resolution is influenced by optical aberrations, alignment accuracy, finite camera pixel size, image sampling, and mechanical stability.

Among the four imaging configurations, the side imaging system operating at $M = 0.6$ achieved the lowest experimental resolution, resolving features up to Group 5, Element 2. Both top imaging systems showed improved performance by resolving Group 5, Element 5, corresponding to an experimental resolution of approximately 9.8 μm. The highest resolving capability was achieved by the side imaging system operating at $M = 10$, which successfully resolved Group 6, Element 3, corresponding to an experimental resolution of approximately 6.2 μm. These results are consistent with the intensity profile analysis presented in the previous section, where the higher-magnification imaging systems maintained stronger modulation and better separation between adjacent peaks at higher spatial frequencies.

Overall, the theoretical calculations and experimental measurements demonstrate that the four imaging configurations provide progressively improved resolving capability as the imaging magnification increases. Together with the magnification calibration, these measurements establish the performance of the imaging systems and provide the quantitative calibration required for future absorption imaging of magneto-optical traps and Bose–Einstein condensates.

Chapter 6

Discussion and Conclusions

6.1 Discussion

The work presented in this thesis extends beyond the development of an optical imaging system and establishes an experimental platform for future investigations of ultracold sodium atoms and spinor Bose–Einstein condensates. The successful integration of the ultrahigh-vacuum apparatus, laser cooling and trapping system, magnetic-field control electronics, and calibrated imaging system demonstrates that reliable ultracold atom experiments require the coordinated performance of multiple experimental subsystems. As the complexity of quantum gas experiments continues to increase, the integration and optimization of these individual components have become equally as important as advances in atomic manipulation itself [39, 40].

A central outcome of this work is the successful implementation and quantitative characterization of the imaging system, which serves as the primary diagnostic tool for future experiments. Although imaging represents the final stage of an experimental sequence, nearly all measurable physical quantities, including cloud size, atom number, optical density, condensate fraction, and spin populations, ultimately depend on the accuracy of the imaging process. Consequently, the calibration of magnification and spatial resolution performed in this work provides the foundation for all future quantitative measurements using the sodium apparatus. Rather than relying solely on theoretical optical design, the experimental validation confirms that the assembled system performs close to its intended specifications under realistic laboratory conditions.

The experimental results also demonstrate the importance of balancing theoretical optical performance with practical engineering considerations. While the measured spatial resolution is modestly worse than the theoretical diffraction limit, the difference remains consistent with the performance expected from multi-element relay imaging systems operating through vacuum viewports. Such deviations arise naturally from residual aberrations, finite detector sampling,

and unavoidable mechanical tolerances, emphasizing that experimentally calibrated performance provides a more meaningful assessment of an imaging system than theoretical diffraction limits alone. Similar conclusions have been reached in a wide range of modern quantum gas experiments, where careful experimental characterization is considered essential for achieving reproducible and quantitative measurements [41, 42].

Beyond validating the current apparatus, this work establishes a flexible experimental framework for future research. The modular optical design allows straightforward implementation of higher numerical aperture objectives, advanced scientific cameras, adaptive wavefront correction, and alternative imaging techniques without major modification of the existing experimental platform. Consequently, the infrastructure developed in this thesis provides not only the capability for routine absorption imaging of sodium magneto-optical traps but also the foundation for future investigations of Bose–Einstein condensation, coherent spin dynamics, quantum simulation, and many-body phenomena in ultracold atomic gases. In this sense, the contributions of this thesis represent an important step toward expanding the experimental capabilities of the laboratory and enabling a broad range of future studies in atomic, molecular, and optical physics.

6.2 Performance of the Imaging System

The successful characterization of the imaging system represents one of the principal outcomes of this thesis because it establishes the quantitative relationship between the designed optical performance and the behavior of the experimentally assembled apparatus. While the optical system was initially designed using paraxial ray-tracing principles and computer-aided mechanical modeling, the true performance of any imaging system can only be determined through experimental validation. Every optical component, including relay lenses, vacuum viewports, mirrors, filters, and the detector itself, contributes to the final image quality. Consequently, the experimentally measured magnification and spatial resolution provide the most meaningful assessment of whether the imaging system satisfies the requirements for future absorption imaging of ultracold sodium atoms. Modern ultracold atom experiments similarly emphasize experimental calibration as an essential component of imaging-system development rather than relying solely on theoretical optical predictions [43, 44, 35].

One of the most encouraging results obtained during this work is the excellent agreement between the designed and experimentally measured magnification. The experimentally determined magnification of 0.653 ± 0.033 differed only slightly from the nominal design value of approximately $0.6\times$. Such agreement indicates that the optical design methodology adopted during the CAD

development stage successfully translated into the physical implementation of the imaging system. It also demonstrates that the mechanical mounting strategy maintained the relative spacing between successive optical elements with sufficient precision to preserve the designed image formation. Because magnification directly determines the conversion between detector pixels and object-plane dimensions, this calibration establishes the physical length scale for every subsequent measurement performed with the imaging system. Similar calibration procedures have become standard practice in quantitative absorption imaging because uncertainties in magnification propagate directly into measurements of cloud size, atomic density, and atom number [35, 43].

The small deviation between the theoretical and measured magnification should not be interpreted as evidence of imperfect optical design. Rather, such deviations are expected in practical laboratory systems. Thin-lens calculations assume perfectly known focal lengths, ideal lens positioning, negligible manufacturing tolerances, and perfectly aligned optical axes. In reality, commercially manufactured achromatic lenses possess finite tolerances in focal length and surface figure, while optomechanical mounts introduce positioning uncertainties on the order of tens to hundreds of micrometers. When several optical components are combined into a relay imaging system, these individual uncertainties accumulate and produce small deviations from the nominal design parameters. The experimentally measured magnification therefore reflects the performance of the complete optical instrument rather than the idealized theoretical model used during its design [44, 43].

In addition to improving optical performance, the redesigned imaging system provides substantial mechanical advantages over the previous laboratory configuration. The earlier imaging system was constructed directly on the optical table using individual optical mounts, making the alignment sensitive to small mechanical disturbances and requiring periodic realignment of the imaging optics. In the present design, all relay lenses are mounted on rigid optical rail systems that preserve the relative spacing between successive optical components. Consequently, the object plane, image plane, and focal positions remain fixed once the system has been aligned, greatly reducing alignment drift over time. The rail-based architecture therefore provides improved mechanical rigidity, enhanced reproducibility, and greater long-term stability while simplifying maintenance and future modifications to the imaging system. These characteristics are particularly valuable in ultracold atom experiments, where stable optical alignment is essential for obtaining reproducible absorption images over extended experimental campaigns.

The resolution measurements provide an even more important evaluation of the completed imaging system because spatial resolution ultimately determines the smallest experimentally

observable features within an ultracold atomic cloud. Theoretical calculations based on the Rayleigh criterion predicted a diffraction-limited resolution of approximately 7.2 μm, whereas experimental characterization using the USAF 1951 resolution target yielded a practical resolution of approximately 13.9 μm. Although the experimental resolution is approximately twice the theoretical diffraction limit, this level of agreement is consistent with expectations for practical relay imaging systems employing commercial optical components, vacuum windows, and CCD detectors. Contemporary ultracold atom imaging systems similarly report that experimentally measured resolutions frequently exceed the ideal diffraction limit because multiple sources of systematic degradation contribute simultaneously to image formation [45, 44].

An important consideration when interpreting this difference is that the Rayleigh criterion represents an idealized physical limit rather than an experimentally expected value. The theoretical diffraction limit assumes monochromatic illumination, aberration-free optics, perfect wavefront quality, infinitely small detector pixels, and ideal alignment throughout the optical system. None of these assumptions are completely satisfied in laboratory experiments. Instead, every practical imaging system experiences additional broadening of the point spread function arising from residual optical aberrations, finite detector sampling, scattered light, mechanical instability, and imperfect optical alignment. Consequently, the experimentally measured resolution should be viewed as the combined performance of the entire imaging chain rather than a direct test of diffraction theory itself [45, 44].

Among these various factors, residual optical aberrations are likely the dominant contribution to the measured resolution. Even though achromatic doublets substantially reduce chromatic aberration, they cannot completely eliminate spherical aberration, coma, astigmatism, field curvature, and distortion. Furthermore, the imaging beam traverses several vacuum viewports before reaching the detector. Optical flats and vacuum windows frequently introduce small wavefront distortions resulting from residual stress during fabrication or mounting. Although these aberrations are often negligible for low-resolution imaging, they become increasingly important when attempting to approach diffraction-limited performance. Recent work has demonstrated that aberrations introduced by vacuum windows frequently represent one of the dominant limitations in ultracold atom microscopy and that digital wavefront correction can substantially improve the effective resolution of existing imaging systems without replacing optical hardware [45, 46].

The intensity-profile analysis performed using progressively finer elements of the USAF 1951 resolution target provides additional insight into the imaging performance beyond the single numerical resolution value. Rather than relying solely on visual inspection of the target, the

extracted line profiles demonstrate the gradual degradation of image contrast as the spatial frequency approaches the resolution limit. Lower-frequency elements exhibit well-defined intensity maxima and minima corresponding to clearly resolved bright and dark bars, whereas higher-frequency elements display progressively reduced modulation depth until adjacent features become indistinguishable. This continuous transition reflects the finite modulation transfer characteristics of the imaging system and provides a more physically meaningful description of image quality than a simple pass-or-fail resolution threshold [43, 44].

6.3 Limitations of the Current Imaging System

Although the imaging system performed close to its design specifications, several practical factors prevented it from achieving the theoretical diffraction-limited resolution. The measured resolution of approximately 13.9 μm was larger than the theoretical value of 7.2 μm, which is expected for a laboratory imaging system. Residual optical aberrations, slight alignment errors, finite detector pixel size, and imperfections introduced by vacuum viewports all contribute to broadening the effective point spread function, resulting in a practical resolution that is typically larger than the ideal diffraction limit predicted by the Rayleigh criterion [46]. In addition, the characterization was performed using a USAF 1951 resolution target rather than an actual ultracold sodium cloud. Consequently, the measured performance represents the intrinsic capability of the optical system and does not include experimental factors such as photon shot noise, probe beam fluctuations, or optical density variations that will be present during absorption imaging of trapped atoms [35].

Despite these limitations, the imaging system satisfies the requirements for its intended application. The experimentally measured magnification agrees well with the optical design, and the achieved spatial resolution is sufficient to accurately determine the size, position, and optical density of sodium magneto-optical traps. Furthermore, the modular optical layout provides flexibility for future upgrades, including higher numerical aperture objectives, improved detectors, and adaptive wavefront correction techniques, should future Bose–Einstein condensate experiments require higher spatial resolution [45].

6.4 Outlook and Future Work

The successful characterization of the imaging system marks the completion of the first phase of its development and provides the confidence required to proceed to experiments with ultracold sodium atoms. Throughout this work, the optical performance was evaluated using a standardized USAF 1951 resolution target, allowing the magnification, spatial resolution, and overall image

quality to be quantified under controlled conditions. These measurements verified that the system performs close to its design specifications and is suitable for quantitative imaging applications.

The next stage of this project will involve performing absorption imaging of a magneto-optical trap (MOT). Unlike the resolution target used in this study, a trapped atomic cloud presents additional experimental challenges, including finite optical density, photon shot noise, probe beam intensity fluctuations, and variations in atom number. Consequently, imaging the MOT will provide the first opportunity to evaluate the performance of the complete imaging system under realistic experimental conditions. Parameters such as cloud size, atom number, optical density, and signal-to-noise ratio will be compared with the expected performance of the optical design to further validate the imaging system.

Following successful MOT imaging, the calibrated imaging platform will be applied to Bose–Einstein condensation experiments. Accurate absorption imaging will enable quantitative measurements of condensate formation, cloud expansion during time-of-flight, and atomic density distributions. Ultimately, the imaging system will support investigations of coherent spin dynamics in sodium spinor Bose–Einstein condensates, including spin-domain formation, spin-mixing dynamics, and other many-body quantum phenomena. The experimental infrastructure established in this thesis therefore provides not only a validated imaging system but also the foundation for a broad range of future studies in ultracold atomic physics.

6.5 Conclusions

This thesis presented the design, implementation, and experimental characterization of an optical imaging system for ultracold sodium atom experiments. By integrating the imaging system with the existing ultrahigh-vacuum apparatus, laser cooling infrastructure, and magnetic-field control electronics, a complete experimental platform was established for future studies of magneto-optical trapping and spinor Bose–Einstein condensates. Experimental measurements demonstrated that the imaging system achieved a magnification consistent with the optical design and a spatial resolution of approximately 13.9 μm, in reasonable agreement with the theoretical diffraction-limited prediction. The systematic characterization of magnification, spatial resolution, and imaging performance confirms that the system is capable of quantitative absorption imaging and provides a reliable foundation for future experiments. Moving forward, this calibrated imaging platform will enable detailed investigations of sodium MOTs, Bose–Einstein condensates, and coherent spin dynamics, while also serving as a flexible framework for future improvements and advanced imaging techniques.

Bibliography

[1] K. B. Davis et al. Bose–einstein condensation in a gas of sodium atoms. *Physical Review Letters*, 75:3969–3973, 1995.

[2] M. H. Anderson et al. Observation of bose–einstein condensation in a dilute atomic vapor. *Science*, 269:198–201, 1995.

[3] C. J. Foot. *Atomic Physics*. Oxford University Press, 2005.

[4] D. A. Steck. Sodium d line data, 2003.

[5] L. W. Anderson and A. T. Ramsey. Study of the spin relaxation times and the effects of spin exchange collisions in an optically oriented sodium vapor. *Physical Review*, 132:712–720, 1963.

[6] T.-L. Ho. Spinor bose–einstein condensates in optical traps. *arXiv preprint cond-mat/9904034*, 1999.

[7] D. M. Stamper-Kurn and M. Ueda. Spinor bose gases: Symmetries, magnetism, and quantum dynamics. *Reviews of Modern Physics*, 85:1191–1244, 2013.

[8] D. McCarron. Laser cooling and trapping molecules. *Journal of Physics B: Atomic, Molecular and Optical Physics*, 51:212001, 2018.

[9] C. Adams and I. Hughes. Laser cooling and trapping. In *Handbook of Laser Technology and Applications*, pages 127–138. CRC Press, 2021.

[10] R. H. Shepard et al. Optical design and characterization of an advanced computational imaging system. *Proc. SPIE*, 9216:73–87, 2014.

[11] B. Welz and M. G. R. Vale. Atomic absorption spectrometry and related techniques. In *Ewing's Analytical Instrumentation Handbook*, pages 71–116. CRC Press, 2019.

[12] I. López-García and M. Hernández-Córdoba. Atomic absorption spectrometry. In *Handbook of Mineral Elements in Food*, pages 189–217. Springer, 2015.

[13] T. Pfrommer and P. Hickson. High resolution mesospheric sodium properties for adaptive optics applications. *Astronomy & Astrophysics*, 565:A102, 2014.

[14] C. Gross and W. S. Bakr. Quantum gas microscopy for single atom and spin detection. *Nature Physics*, 17:1316–1323, 2021.

[15] N. Moussaoui, F. Djaidri, and F. Z. Ouanoufi. Some characteristics of the e-elt sodium lgss. *Acta Physica Polonica A*, 137:496–498, 2020.

[16] Y. Kawaguchi and M. Ueda. Spinor bose–einstein condensates. *Physics Reports*, 520(5):253–381, 2012.

[17] C. K. Law, H. Pu, and N. P. Bigelow. Quantum spins mixing in spinor bose–einstein condensates. *Physical Review Letters*, 81(24):5257–5261, 1998.

[18] H. Pu, C. K. Law, S. Raghavan, J. H. Eberly, and N. P. Bigelow. Spin-mixing dynamics of a spinor bose–einstein condensate. *Physical Review A*, 60(2):1463–1470, 1999.

[19] W. Zhang, D. L. Zhou, M. S. Chang, M. S. Chapman, and L. You. Coherent spin mixing dynamics in a spin-1 atomic condensate. *Physical Review A*, 72:013602, 2005.

[20] L. Zhao, J. Jiang, T. Tang, M. Webb, and Y. Liu. Dynamics in spinor condensates tuned by a microwave dressing field. *Physical Review A*, 89:023608, 2014.

[21] I. Morgenstern, S. Zhong, Q. Zhang, L. Baker, J. Norris, B. Tran, and A. Schwettmann. A versatile microwave source for cold atom experiments controlled by a field programmable gate array. *Review of Scientific Instruments*, 91:023202, 2020.

[22] C. Gross, T. Zibold, E. Nicklas, J. Estève, and M. K. Oberthaler. Nonlinear atom interferometer surpasses classical precision limit. *Nature*, 464:1165–1169, 2010.

[23] C. D. Hamley, C. S. Gerving, T. M. Hoang, E. M. Bookjans, and M. S. Chapman. Spin-nematic squeezed vacuum in a quantum gas. *Nature Physics*, 8:305–308, 2012.

[24] B. Lücke, M. Scherer, J. Kruse, L. Pezzé, F. Deuretzbacher, P. Hyllus, O. Topic, J. Peise, W. Ertmer, J. Arlt, L. Santos, A. Smerzi, and C. Klempt. Twin matter waves for interferometry beyond the classical limit. *Science*, 334(6057):773–776, 2011.

[25] C. S. Gerving, T. M. Hoang, B. J. Land, M. Anquez, C. D. Hamley, and M. S. Chapman. Non-equilibrium dynamics of an unstable quantum pendulum explored in a spin-1 bose–einstein condensate. *Nature Communications*, 3:1169, 2012.

[26] S. Q. Shang, Z. T. Lu, and S. J. Freedman. Comparison of the cold-collision losses for laser-trapped sodium in different ground-state hyperfine sublevels. *Physical Review A*, 50(6):R4449–R4452, 1994.

[27] K. Nasyrov, V. Biancalana, A. Burchianti, R. Calabrese, C. Marinelli, E. Mariotti, and L. Moi. Magneto-optical trap operating on a magnetically induced level mixing effect. *Physical Review A*, 64(2):023412, 2001.

[28] E. L. Raab, M. Prentiss, A. Cable, S. Chu, and D. E. Pritchard. Trapping of neutral sodium atoms with radiation pressure. *Physical Review Letters*, 59:2631–2634, 1987.

[29] Min-Seok Chang. *Coherent Spin Dynamics of a Spin-1 Bose-Einstein Condensate*. PhD thesis, Georgia Institute of Technology, 2006.

[30] Maria Pappa. *Imaging Bose-Einstein Condensates at Ultra-Low Atom Numbers and Time Averaged Adiabatic Potentials*. PhD thesis, University of Crete, 2011.

[31] Thomas B. Ottenstein. *A New Objective for High Resolution Imaging of Bose-Einstein Condensates*. PhD thesis, Kirchhoff Institute of Physics, Heidelberg University, 2006.

[32] Eugene Hecht. *Optics*. Pearson, 5 edition, 2017.

[33] Max Born and Emil Wolf. *Principles of Optics*. Cambridge University Press, 7 edition, 1999.

[34] E. W. Streed, A. Jechow, B. G. Norton, and D. Kielpinski. Absorption imaging of a single atom. *Nature Communications*, 3:933, 2012.

[35] K. Hueck, N. Luick, L. Sobirey, J. Siegl, T. Lompe, H. Moritz, L. W. Clark, and C. Chin. Calibrating high intensity absorption imaging of ultracold atoms. *Optics Express*, 25(8):8670–8682, 2017.

[36] Michael R. White. *Ultracold Atoms in a Disordered Optical Lattice*. PhD thesis, University of Illinois at Urbana-Champaign, 2009.

[37] John R. Taylor. *An Introduction to Error Analysis: The Study of Uncertainties in Physical Measurements*. University Science Books, 2 edition, 1997.

[38] Philip R. Bevington and D. Keith Robinson. *Data Reduction and Error Analysis for the Physical Sciences*. McGraw-Hill, 3 edition, 2003.

[39] Maciej Lewenstein, Anna Sanpera, Verònica Ahufinger, Bogdan Damski, Aditi Sen, and

Ujjwal Sen. Ultracold atomic gases in optical lattices: Mimicking condensed matter physics and beyond. *Advances in Physics*, 56(2):243–379, 2007.

[40] Christian Gross and Immanuel Bloch. Quantum simulations with ultracold atoms in optical lattices. *Science*, 357(6355):995–1001, 2017.

[41] Antoine Browaeys and Thierry Lahaye. Many-body physics with individually controlled rydberg atoms. *Nature Physics*, 16:132–142, 2020.

[42] Matthew A. Norcia, Aaron W. Young, and Adam M. Kaufman. Microscopic control and detection of ultracold atoms in optical-tweezer arrays. *Nature Reviews Physics*, 5:483–495, 2023.

[43] Gal Ness, Anastasiya Vainbaum, Constantine Shkedrov, Yanay Florshaim, and Yoav Sagi. Single-exposure absorption imaging of ultracold atoms using deep learning. *Physical Review Applied*, 14(1):014011, 2020.

[44] Tong Liu, Yifan Li, Xiaoyu Zhang, et al. High-precision characterization and calibration of cold-atom imaging systems. *Physical Review Applied*, 20:014037, 2023.

[45] Emine Altuntas and Ian B. Spielman. Self-bayesian aberration removal via constraints for ultracold atom microscopy. *Physical Review Applied*, 17(5):054061, 2022.

[46] Paul Hill, Philipp Lunt, Johannes Reiter, Maciej Gałka, Philipp M. Preiss, and Selim Jochim. Optical phase aberration correction with an ultracold quantum gas. *Physical Review A*, 110:053308, 2024.